nature communications

Article

https://doi.org/10.1038/s41467-025-61914-8

Stem cell secretome armed magneto-actuated micromotors as spatio-temporal manipulators for wound healing acceleration

Received: 15 August 2024

Accepted: 3 July 2025

Published online: 22 July 2025

Check for updates

Jiamiao Jiang[1,6], Haiying Liang[1,6], Yicheng Ye[1], Weichang Huang[1,2], Jiajun Miao[1], Haixin Tan[1], Ziwei Hu[1], Hao Tian[1], Hanfeng Qin[1], Xiaoting Zhang[1], Lishan Zhang[1], Junbin Gao[1], Xian Shen[3] ✉, Shuanghu Wang[4] ✉, Fei Peng[5] ✉ & Yingfeng Tu[1] ✉

Healing complex wounds, especially deep injuries, requires therapies that can target different healing phases while penetrating physical barriers like fibrin clots and scab. Existing approaches fail to fully address these spatiotemporal challenges due to reliance on passive drug diffusion. Here, we develop magnetic microspheres loaded with therapeutic factors derived from stem cells (collectively called the "secretome") to actively guide wound repair. These microspheres provide sustained release of bioactive factors and can be precisely navigated using external magnetic fields. In vitro, they exhibit potent anti-inflammatory effects and progressively enhance skin cell proliferation and migration. Unlike conventional therapies, magnetic propulsion allows them to penetrate dense wound barriers more effectively. In male murine full-thickness wounds, the micromotors accelerate healing by promoting tissue regeneration, reducing inflammation, and improving collagen and blood vessel formation. Successful results in male pigs further confirm their cross-species potential. By combining magnetic mobility with a composite bioactive secretome, this platform overcomes both spatial and temporal limitations in wound treatment.

As the primary barrier maintaining physiological homeostasis and defending against external pathogens, the skin's capacity to repair and regenerate remains a central challenge in regenerative medicine[1,2]. Cutaneous tissues, constantly exposed to environmental stressors, require precisely coordinated healing phases of hemostasis, inflammation, proliferation, and remodeling to restore integrity[3,4]. However, micro-environmental imbalances such as persistent inflammation, secondary infection, or oxidative stress frequently disrupt this process. While superficial wounds often heal completely with proper care, deep tissue injuries frequently progress to chronic non-healing ulcers due to bacterial colonization and dysregulated repair, posing life-threatening risks[5–7]. Notably, the global aging population has exacerbated the prevalence of chronic wounds, underscoring the urgency for precision therapies targeting deep-tissue damage[8,9].

The pathophysiological complexity of deep cutaneous wounds manifests in two dimensions: (1) the need for synergistic interventions

[1]Guangdong Provincial Key Laboratory of New Drug Screening, School of Pharmaceutical Sciences, Southern Medical University, Guangzhou, China. [2]Department of Pulmonary and Critical Care Medicine, The Second Affiliated Hospital of Guangzhou Medical University, Guangzhou, China. [3]Department of General Surgery, The First Affiliated Hospital of Wenzhou Medical University, Wenzhou, China. [4]Central Laboratory of Lishui Hospital of Wenzhou Medical University, The First Affiliated Hospital of Lishui University, Lishui People's Hospital, Lishui, China. [5]School of Materials Science and Engineering, Sun Yat-Sen University, Guangzhou, China. [6]These authors contributed equally: Jiamiao Jiang, Haiying Liang. ✉e-mail: 13968888872@163.com; wangshuanghu@lsu.edu.cn; pengf26@mail.sysu.edu.cn; tuyingfeng1@smu.edu.cn

across inflammatory regulation, angiogenesis, and matrix remodeling[10–13], and (2) physical barriers like fibrin clots, scars and biofilms that impede therapeutic penetration[14–16]. These challenges create dual therapeutic contradictions—balancing complex healing demands with synergistic interventions, while overcoming penetration barriers for deep tissue targeting.

Modern wound care has evolved from passive protection to active modulation strategies. Conventional dressings fail to address time-phased synergistic intervention requirements, while growth factor therapies suffer from burst release limitations[17,18]. Emerging technologies—smart dressings, stem cell therapies, and extracellular matrix mimics—partially resolve temporal challenges through multifunctional designs[19–22]. Nanoparticle and hydrogel systems improve drug loading but remain constrained by passive diffusion mechanisms[23]. This spatiotemporal paradox is particularly pronounced in chronic wounds (e.g., diabetic ulcers) and full-thickness defects, demanding interdisciplinary innovation.

Stem cells, specifically mesenchymal stem cells (MSCs), owing to the abilities of self-renewal and multidirectional differentiation, have emerged as promising tools for tissue repair[24,25]. However, clinical translation is hindered by low post-transplant viability and unpredictable differentiation[26,27]. Emerging evidence indicates that MSC therapeutic effects primarily stem from paracrine signaling rather than cellular engraftment[28–30]. The MSC secretome encompassing growth factors, cytokines, and microRNAs within conditioned medium (CM)[31,32], has demonstrated therapeutic efficacy in colitis, hepatic fibrosis, bone regeneration and angiogenesis[33–35]. While CM demonstrates composite bioactive in regulating wound microenvironments, its clinical utility is limited by short half-life and poor tissue penetration[36].

Micro/nanomotors (MNMs), capable of converting external energy into autonomous motion. These dynamic systems have emerged as transformative tools in biomedical applications, particularly for targeted delivery and overcoming physiological barriers[37–41]. In wound healing contexts, MNMs demonstrate exceptional therapeutic potential by enhancing tissue penetration efficiency through self-propulsion mechanisms. Chemically powered nanomotors utilize catalytic decomposition of hydrogen peroxide to generate oxygen bubbles, propelling directional movement that enables biofilm disruption and deep tissue infiltration[42]. Near-infrared-responsive nanomotors with umbrella-like architectures achieve transdermal drug penetration via photothermal propulsion, precisely targeting infected regions[43]. Biohybrid Microrobots incorporating microalgae exhibit enhanced thrombus permeability through autonomous motion, facilitating prolonged tissue retention[44]. Magnetically driven MNMs, incorporating magnetic components, have become a predominant focus due to their non-invasive controllability, deep tissue penetration, and biocompatibility[45–48]. Recent advances in gradient magnetic field-guided biohybrid nanoparticles significantly improve diabetic wound repair through enhanced tissue penetration[49]. Therefore, magnetic field-driven systems transcend traditional drug delivery limitations, offering innovative solutions for spatiotemporally precise wound management.

To address the dual challenges of insufficient synergistic intervention and limited physical barrier penetration in deep wound repair, we developed a magnetically propelled micromotor system (CSFCM + M) functionalized with MSC secretome components (Fig. 1). This platform combined CM for sustained factor release with magnetic navigation capabilities for active tissue penetration. In vitro studies confirmed CSFCM's dual functionality: enhancing keratinocyte proliferation/migration while suppressing inflammatory cascades. Under rotating magnetic fields, CSFCM + M micromotors achieved controllable navigation, actively penetrating simulated thrombus barriers —a critical advancement over conventional diffusion limited delivery systems. In murine full-thickness defect models, CSFCM + M micromotors actively infiltrating granulation tissue through scab fissures, coordinating accelerated healing processes: rapid wound closure, improved epidermal regeneration, anti-inflammatory activity, and enhanced collagen deposition/angiogenesis. Consistent therapeutic outcomes were replicated in porcine models anatomically analogous to human skin, confirming clinical translation potential. By integrating MSC paracrine signaling with magnetically enhanced delivery, this work opens up avenues for intelligent wound management systems that synchronize biological activity with spatiotemporal precision.

Results

Fabrication and Characterization of CSFCM

MSCs used in this study were obtained from the mouse bone marrow tissue (BM-MSCs) and the collected BM-MSCs were cultured in MEM Alpha basic medium (α-MEM) supplemented with 10% fetal bovine serum (FBS) at 37 °C[50]. After three passages (P3), BM-MSCs exhibited a fibroblast-like morphology (Supplementary Fig. 1) and flow cytometry was then used to identify BM-MSCs by quantifying the level of surface cell markers. Flow cytometry assay for cell surface antigens showed positive results for Sca-1, CD105, CD90 (Thy1.2), CD44 and negative results for CD45 and CD34, which are consistent with previous report (Supplementary Figs. 2, 3)[51–53]. It is worth noting that the reported positivity rates for surface markers in murine BM-MSCs vary significantly across different studies, and the positive rates of Sca-1 (55.33%) and Thy1.2 (37.05%) in the literature were much lower than our results, which were 99.0% for Sca-1 and 42.0% for Thy1.2[52]. Moreover, osteogenic and lipogenic differentiation induction results also showed the ability of the cells to differentiate in a directed manner (Supplementary Fig. 4). Overall, the obtained cells have the characteristics of BM-MSCs. BM-MSCs at passages 3-5 were used in our study to guarantee the cell quality. To obtain CM of BM-MSCs, the cells were cultured in serum-free α-MEM medium for 2 days. And the medium was collected for centrifugation at 300 × *g* for 5 min, then sterilized with 0.22 μm syringe filter and freeze-dried for further usage[36].

To endow micromotors with magnetic responsiveness, magnetic nanoparticles (F) were first synthesized by atmospheric pressure solvothermal method[54]. Transmission electron microscope (TEM) images showed that the as-synthesized F had a nanocluster structure consistent with previous report (Fig. 2A)[54]. Furthermore, magnetic chitosan microspheres loaded with CM (CSFCM) were synthesized through an emulsion crosslinking method[55,56]. Briefly, CS solution containing F and CM was used as aqueous phase, and the resulting aqueous phase was then dropped into the liquid paraffin oil phase under stirring for the formation of water-in-oil emulsion, followed by crosslinking with biocompatible genipin for the fabrication of CSFCM. Magnetic CS microspheres without CM loading (CSF) were prepared similarly. Images taken from inverted microscope showed that the prepared CSF (Supplementary Fig. 5) and CSFCM (Fig. 2B) were uniform microspheres. Scanning electron microscopy (SEM) images further confirmed the microscale spheroidal morphology of these two samples (Supplementary Fig. 6). The size of CSF and CSFCM was then calculated based on SEM images by ImageJ, and the average diameter of CSF was around 2.93 μm and CSFCM was 2.81 μm (Supplementary Fig. 7A). Zeta potential of CSFCM was slightly lower than that of CSF, but still maintained a positive charge (29.43 ± 1.25 mV), favoring the antibacterial effect by electrostatic binding to the negatively charged bacterial cell wall and proinflammatory cytokines (Supplementary Fig. 7B)[57,58]. To confirm the successful loading of CM within CSFCM structure, we first fluorescently labeled CM using the intrinsic reactivity of the fluorescent dye NHS-Cy5 with the primary amine groups present on proteins[59]. The resulting fluorescently labeled CM was then used to synthesize CSFCM. Fluorescence microscopy analysis revealed that the CSFCM particles exhibited a distinct red fluorescence (Supplementary Fig. 8) corresponding to the emission spectrum of Cy5 (λ_{ex} = 649 nm, λ_{em} = 670 nm), confirming the successful encapsulation of CM components into the CSFCM structure. TEM images

https://doi.org/10.1038/s41467-025-61914-8

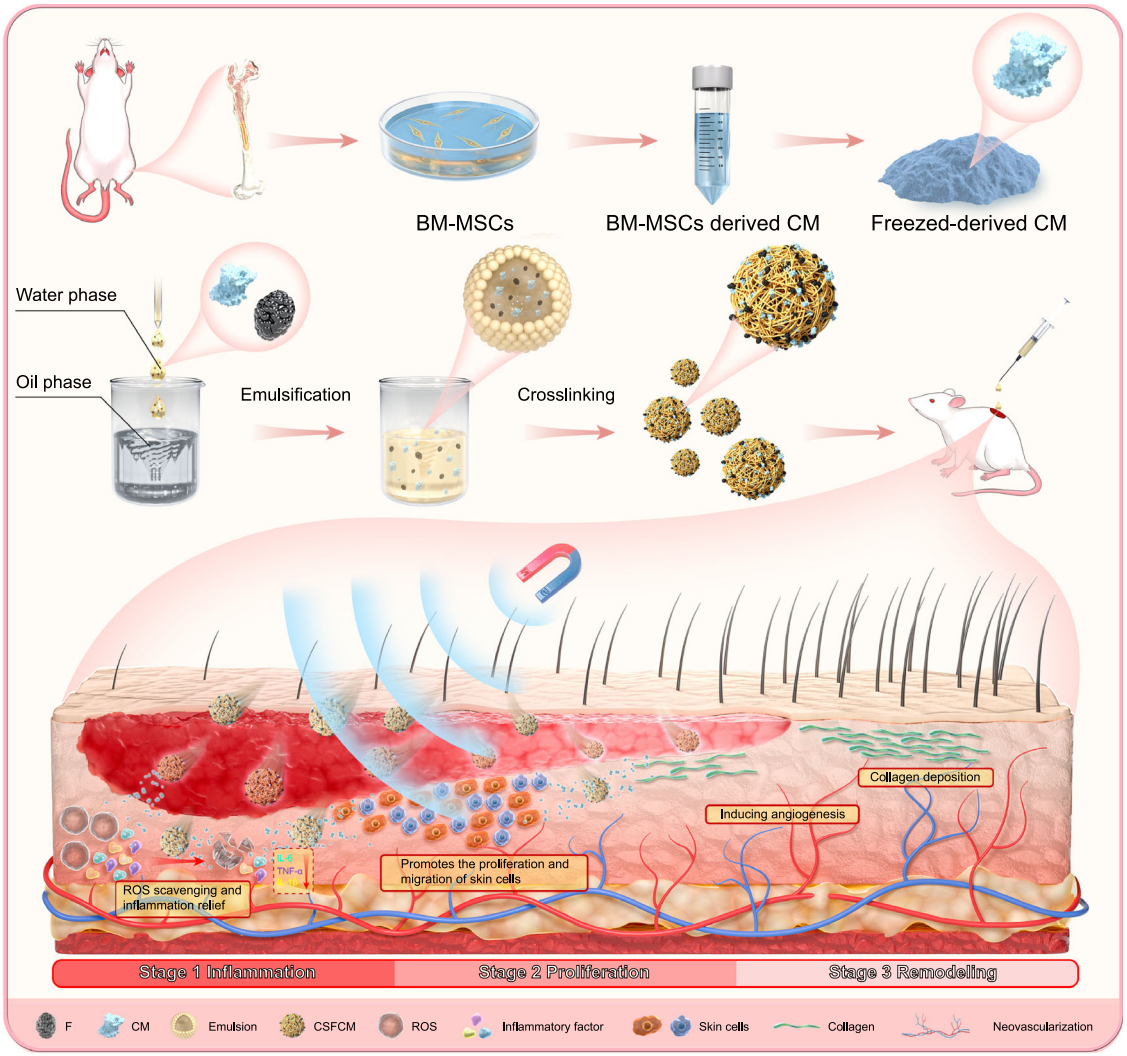

Fig. 1 | Schematic illustration of the CSFCM + M micromotors for spatio-temporally optimized wound healing. CM-functionalized magnetically driven micromotors were prepared by the emulsion cross-linking method. Under a rotating magnetic field, CSFCM + M micromotors were actuated and actively penetrated into deep tissue, ensuring sustained release of bioactive factors in the wound bed. By synchronizing spatial targeting with temporal bioactive modulation, the system coordinated anti-inflammatory, proliferative, and remodeling responses—effectively resolving the dual challenges of physical penetration barriers and insufficient synergistic intervention to accelerate functional tissue regeneration.

(Supplementary Fig. 9, Fig. 2C) of the as-prepared CSF and CSFCM and their local enlarged images (Supplementary Fig. 10) showed that those magnetic F were wrapped in the microspheres, endowing CS microspheres with remote magnetic manipulation ability. The elemental analysis by energy-dispersive spectroscope (EDS) (Supplementary Figs. 11, Fig. 2D) further demonstrated the existence of C, N, O and Fe elements. Powder X-ray diffraction (XRD) measurement was used to verify the successful synthesis of the samples. XRD pattern of F exhibited that the diffraction peaks were closely resembled to the reported magnetite (Fig. 2E)[54]. And XRD spectra of CSF and CSFCM showed strong CS characteristic diffraction peaks around 20°, and displayed weak characteristic diffraction peaks corresponding to magnetite, which could be attributed to the relatively low F loading (Supplementary Figs. 12, Fig. 2E)[60]. The magnetic property of CSF and CSFCM was then measured by vibrating sample magnetometry (VSM, LakeShore 7404) as shown in Supplementary Figs. 13, Fig. 2F, which demonstrated a superparamagnetic property of CSFCM. These results indicated that CM loaded micromotors with magnetic responsiveness were successfully developed.

The protein concentration of CM was quantified by bicinchoninic acid (BCA) protein assay kit (Beyotime, Shanghai, China). The protein encapsulation efficiency and the loading capacity of CSFCM were 48.58% and 16.84%, respectively. Moreover, the release kinetics of CM from CS microspheres were also monitored using BCA kit. As illustrated in Fig. 2G, there was no burst effect in the releasing curve, and the cumulative release amount of CM reached 89.72% on day 6. It is worth mentioning that the loading mode generally influences the release kinetics[55]. Different from the adsorption strategy of drug loading, CM was used as the water phase for direct loading in our system with no burst release and a relatively stable release rate, leading to the continuous release of CM at the wound site. In general, a magnetically responsive micromotor system capable of sustained CM release has been successfully developed, laying a foundation for the deep tissue delivery and prolonged therapeutic availability of bioactive components in damaged skin tissue.

Magnetic actuation of CSFCM and active deep penetration

After confirming the successful fabrication of CSFCM, magnetic actuation was examined further. Under a rotating magnetic field, spherical magnetic microparticles and their assemblies normally rotate near a solid surface. When the rotation axis of these microparticles/assemblies is tilted at an angle, the component of their

https://doi.org/10.1038/s41467-025-61914-8

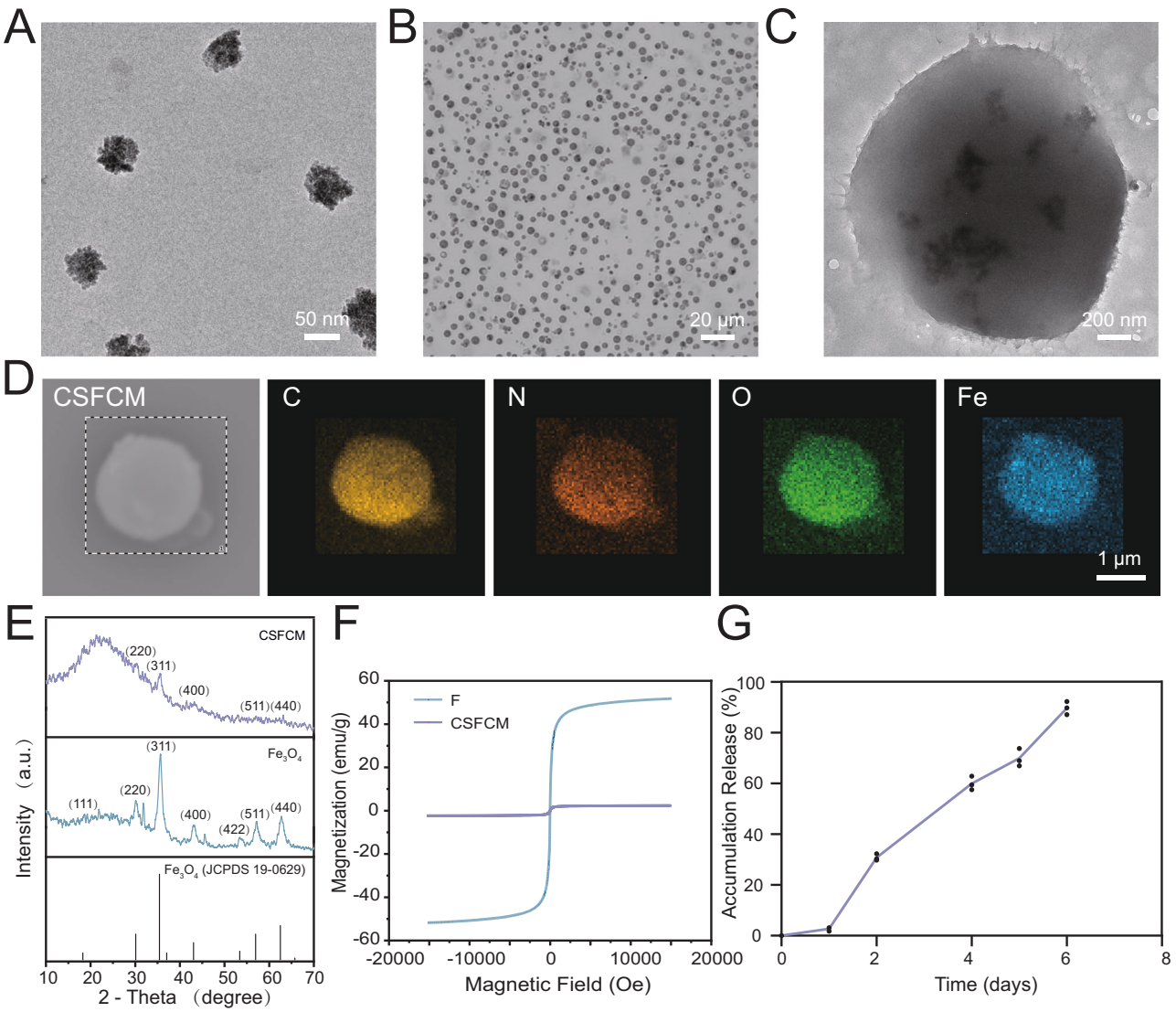

Fig. 2 | Characterizations of CSFCM. A TEM image of magnetic F. **B** Inverted microscope image of CSFCM. **C** TEM image of CSFCM. **D** EDS elemental mappings of CSFCM. **E** XRD patterns of CSFCM and F. **F** Magnetic hysteresis loops of CSFCM and F at room temperature. **G** The cumulative release rate of CM from CSFCM during 6 days ($n = 3$ independent samples). Data are presented as mean ± S.D. Source data are provided as a Source Data file.

rotational motion parallel to the surface converts the rotation into linear translation on the surface through friction[61]. In our system, CSFCM + M spun forward under a rotating magnetic field and responded to magnetic changes with remarkable controllability. It should be noted that the CSFCM + M responded to the magnetic field with a dipole-dipole interaction force, and the neighboring CSFCM microspheres formed a chain-like assembly along the magnetic induction line over time, moving faster than a single microsphere does[62,63]. In the following magnetically driven motion studies, the motion behavior of single microsphere was then recorded by an inverted microscope to demonstrate the law of CSFCM + M magnetically driven motion. Motion trajectories of CSFCM + M with different magnetic frequencies (1, 5, 10, 15, 20, 25, 30, 35, 40, 45, 50, 55, and 60 Hz) were optically tracked as shown in Fig. 3A and the representative motion videos can be seen from Supplementary movie 1. The behavior of active CSFCM + M was closely related to the applied field frequency while the velocity of CSFCM + M increased almost linearly to a peak (6.40 μm·s^{-1}) and subsequently decreased as the frequency further increased (Fig. 3B), which was consistent with the motion behavior of the reported magnetic micromotors[64]. The frequency at which the speed reached its maximum in this case 15 Hz is called step-out frequency. When the driving frequency rose from 1 to 15 Hz, the velocity of CSFCM + M increased from 1.74 to 6.40 μm·s^{-1}, whereas it decreased to 2.24 μm·s^{-1} as the frequency further increased to 60 Hz. The mean square displacement (MSD) under different magnetic frequencies was then calculated with a parabolic-like function curve (Fig. 3C and Supplementary Fig. 14), which reflected the directional motion of CSFCM + M. The slope of the curve represented the motion speed, which conformed to the above-mentioned law of speed changing with frequency. Moreover, the directional motion of CSFCM + M wirelessly controlled by rotating magnetic field was also investigated. Under magnetic manipulation, CSFCM + M were steered to travel along a predetermined path (Supplementary movie 2), and the square trajectories can be written in Fig. 3D. In summary, CSFCM + M were capable of magnetic actuation with highly controllable direction and speed.

We have also investigated the ability of CSFCM + M to penetrate deep blood clots under magnetic guidance. CSFCM were labeled with Rhodamine B (RhB-CSFCM) to verify the penetration of micromotor into simulated thrombus under magnetic field. 3, 3′-dioctadecyloxacarbocyanine perchlorate (DIO)-labeled simulated thrombus (green fluorescence) was first prepared in a confocal dish, and RhB-CSFCM with

https://doi.org/10.1038/s41467-025-61914-8

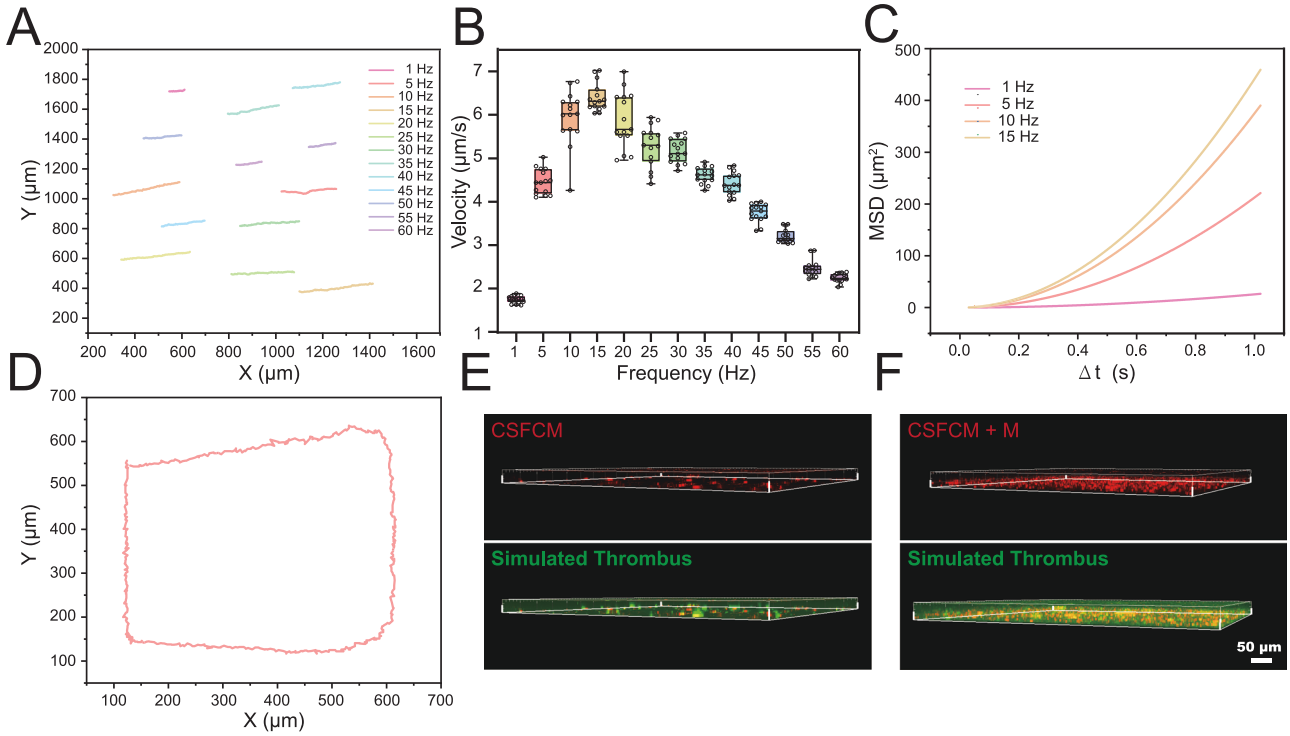

Fig. 3 | Motion behavior of CSFCM + M. A Optical tracking trajectories of CSFCM + M at different magnetic frequencies. **B** Velocity of CSFCM + M under different magnetic frequencies. Result in **B** was shown as box plots, the box bounds indicate the 25th percentiles (lower quartiles, Q1) and 75th percentiles (upper quartiles, Q3) and the box represents the interquartile range (IQR), while the whiskers extend to the minimum and maximum values within the IQR, the center line of the box indicating the median. All individual data points are displayed in the box plot. **C** MSD curves of CSFCM + M at different frequencies. ($n = 15$ independent samples). **D** Writing square trajectory by adjusting magnetic field in 5 Hz. **E, F** 3D fluorescence images of simulated thrombus penetrated by CSFCM and CSFCM + M, respectively. Experiments were performed three times. Source data are provided as a Source Data file.

a concentration of 250 μg·mL^{-1} were added to the dishes, followed by magnetic treatment for 20 min, while RhB-CSFCM without magnetic field was used as the control. After that, the penetration depth of RhB-CSFCM + M (red fluorescence) was determined under a confocal microscope by observing the distribution range of red fluorescent microspheres in green fluorescence, and the results were further analyzed by Imaris 8.1 software. Compared to CSFCM group, CSFCM + M showed 2.23 times more fluorescence intensity in the deep thrombus layer (Fig. 3E, F). The magnetically driven CSFCM + M can penetrate a thrombus constituted of numerous platelets and well-organized fibrin, thanks to the mechanical destruction of cross-linked fibrin, as previously reported[65]. However, the permeation range of CSFCM without magnetic actuation was almost limited to the superficial thrombus layer and rarely entered the deep thrombus layer. Regarding thrombus penetration mechanisms, we propose a hybrid model in which CSFCM + M penetrates simulated thrombus through both coexisting single-particles and assembled states. The magnetic assembly dynamics are governed by several critical parameters, including magnetic field strength, frequency, field duration, particles' magnetic responsiveness, and interparticle distance[62,63]. During time-constrained penetration processes, proximal particles formed assemblies and improved penetration efficiency by mechanically disrupting fibronectin networks, and distal particles remained singular, leveraging smaller hydrodynamic diameters for magnetic propulsion/interstitial migration. In our study, CSFCM + M micromotors deeply penetrated the simulated thrombus through a multi-mode penetration strategy including mechanical disruption, magnetic propulsion, and interstitial navigation.

CSFCM effectively promote skin cell growth and inflammation attenuating

Cell viability was first used to evaluate the biocompatibility of CSF and CSFCM. After 24 h of incubation with varied concentrations of CSF and CSFCM, mouse embryonic fibroblast cells (NIH/3T3 cells) and human keratinocytes cells (HaCaT cells) demonstrated decreasing cell viability with increasing sample concentration (Supplementary Fig. 15). However, because of the presence of CM, CSFCM had higher cell survival than CSF at the same concentration with increased proliferation at low doses (≤ 800 μg·mL^{-1} CSFCM for HaCaT and ≤100 μg·mL^{-1} for NIH/3T3 cells). Therefore, a low dosage of 100 μg·mL^{-1} of CSFCM was used for subsequent cell experiments. The differential responses of NIH/3T3 cells and HaCaT cells to CSFCM may stem from inherent disparities in cellular proliferation kinetics. Experimental observations revealed significantly faster baseline proliferation rates in HaCaT cells compared to NIH/3T3 fibroblasts under standard culture conditions. This fundamental divergence in growth dynamics likely rendered HaCaT cells more responsive to CSFCM during the 24 h treatment window. Conversely, the slower proliferative activity of NIH/3T3 cells may necessitate extended incubation periods to manifest measurable viability changes. Heterogeneity in cell cycle distribution across asynchronous populations could further contribute to variable therapeutic responses, potentially obscuring early-phase treatment effects in slower-cycling NIH/3T3 cells. We then further investigated the effects of different CM concentrations on skin cells proliferation at 24, 48, and 72 h, respectively. As shown in Supplementary Fig. 16, CM could promote the proliferation of both NIH/3T3 cells and HaCaT cells, and the proliferation was more obvious after incubating for 72 h, which was consistent with a previous report[66,67].

In general, the migration and the proliferation of skin cells are essential for epithelial re-formation and tissue remodeling in wound healing. Therefore, the effect of CSFCM on the migratory and proliferative abilities of both fibroblasts and keratinocyte cells was then investigated. The results of the in vitro cell migration assay were shown in Fig. 4A, B, in which the faster the cells on both sides of the scratch migrated to the center, the shorter the distance between the cells. The

https://doi.org/10.1038/s41467-025-61914-8

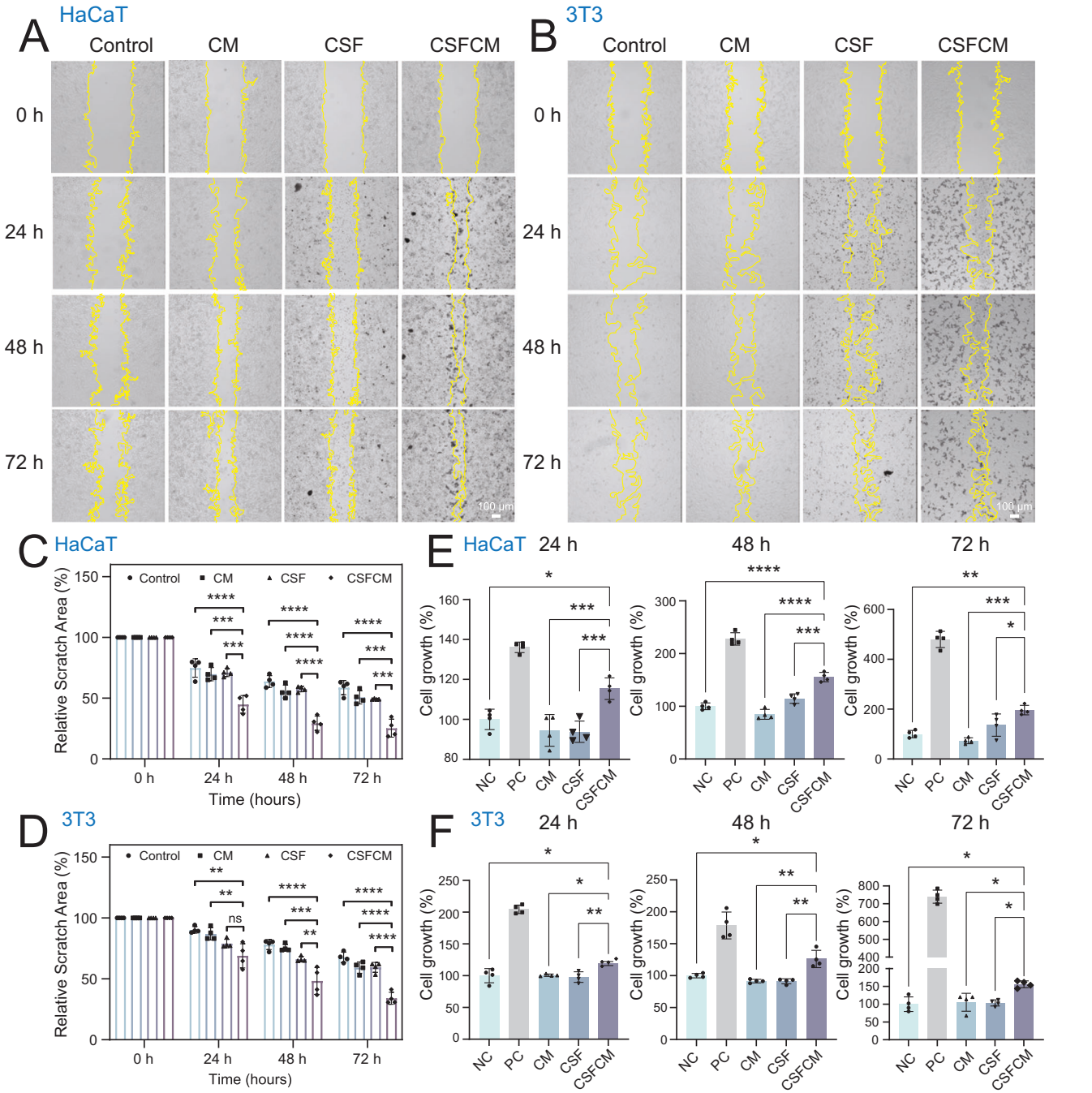

Fig. 4 | Effect of CSFCM on the migration and proliferation of skin cells. Representative cells migration images of HaCaT cells (**A**) and NIH/3T3 cells (**B**) 24, 48, 72 h after CSFCM treatment. Quantitative relative scratch area of HaCaT cells (**C**) and NIH/3T3 cells (**D**). $n = 4$ independent samples. Treatment with basic medium was used as the Control. In Fig. 4C, $^{***}p < 0.001$, $^{****}p < 0.0001$, for the data in 24 h, the exact P value between CSFCM and CM group was 0.0003, and exact p value between CSFCM and CSF group was 0.0002; for the data in 72 h, the exact p value between CSFCM and CM group was 0.0001, and exact P value between CSFCM and CSF group was 0.0002. In Fig. 4D, $^{**}p < 0.01$, $^{***}p < 0.001$, $^{****}p < 0.0001$, for the data in 24 h, the exact P value between CSFCM and Control group was 0.0014, and exact P value between CSFCM and CM group was 0.0053; for the data in 48 h, the exact P value between CSFCM and CM group was 0.0002, and exact P value between CSFCM and CSF group was 0.0066. The proliferation of HaCaT cells (**E**) and NIH/3T3 cells (**F**) quantified by CCK-8 assay, which demonstrated increased proliferation in the CSFCM-treated group compared to the NC group. $n = 4$ independent samples. Negative Control (NC): basic DMEM medium with no FBS; Positive Control (PC): basic DMEM medium with 10% FBS. In Fig. 4E, $^{*}p < 0.05$, $^{**}p < 0.01$, $^{***}p < 0.001$, $^{****}p < 0.0001$, for the data in 24 h, the exact p value between CSFCM and NC group was 0.01, the exact P value between CSFCM and CM group was 0.0007, and exact P value between CSFCM and CSF group was 0.0005; for the data in 48 h, the exact P value between CSFCM and CSF group was 0.0001; for the data in 72 h, the exact P value between CSFCM and NC group was 0.0014, the exact P value between CSFCM and CM group was 0.0001, and exact p value between CSFCM and CSF group was 0.0489. In Fig. 4F, $^{*}p < 0.05$, $^{**}p < 0.01$, for the data in 24 h, the exact P value between CSFCM and NC group was 0.013, the exact P value between CSFCM and CM group was 0.0171, and exact P value between CSFCM and CSF group was 0.0056; for the data in 48 h, the exact P value between CSFCM and NC group was 0.0388, the exact P value between CSFCM and CM group was 0.0051, and exact P value between CSFCM and CSF group was 0.0048; for the data in 72 h, the exact P value between CSFCM and NC group was 0.0236, the exact P value between CSFCM and CM group was 0.0446, and exact P value between CSFCM and CSF group was 0.0364. Data in C-F were presented as mean ± S.D. p values were analyzed by one-way ANOVA with Tukey's multiple comparisons test. Source data are provided as a Source Data file.

quantitative analysis of the relative scratch area reflected the wound healing rate, and our CSFCM possessed significant differences in expediting the wound closure at 24, 48, 72 h (Fig. 4C, D). For HaCaT-cells, the relative scratch area after CSFCM treating for 24 h was 44.91%, whereas the control was 74.90% and the CM-treated group was 69.80%. With the action time of CSFCM prolonging to 72 h, the relative scratch area further decreased to 25.31%, and that of the control was 58.73%, the CM treated group was 50.70% (Fig. 4C). It is worth noting that compared with the control group, CS microspheres without CM could also promote the cells migration to some extent, which may be attributed to the promotive effects of CS on skin fibroblasts and keratinocytes[68,69]. Furthermore, NIH/3T3 cells treated with CSFCM showed a similar cell migration pattern to HaCaT cells (Fig. 4D), suggesting that CSFCM had a good wound closure capacity in vitro. Notably, incomplete scratch closure after 72 h was observed in cell migration assay, which was attributed to the choice of culture medium during the treatment phases. In this experiment, we utilized serum-free base medium as a dispersing solvent for the treatment samples. While some protocols employ complete medium with serum supplementation to maintain baseline proliferation, others (including ours) opt for serum-free basal medium to eliminate potential confounding effects of serum and to isolate the specific effects of therapeutic agents.

The effect of CSFCM on skin cell proliferation was assessed using a CCK8 assay. The results showed a significant increase in HaCaT and NIH/3T3 cell viability in the CSFCM group compared to the FBS-free DMEM treatment group (negative control, NC) and the CM or CSF treatment group. As demonstrated in Fig. 4E, compared to the NC group, HaCaT proliferation was increased by 15.37% after 24 h of CSFCM incubation and by 55.45% and 96.29% after 48 and 72 h of treatment, respectively. Similarly, after CSFCM treatment, NIH/3T3 cell proliferation was also increased by 19.03% at 24 h, 26.20% at 48 h, and 56.07% at 72 h compared to the NC group (Fig. 4F). In general, skin cells treated with CSFCM exhibited a comparable tendency to promote cell proliferation as 10% FBS-containing DMEM treatment group (positive control, PC). The CSFCM system demonstrated progressive enhancement of skin cell proliferation and migration over time, which contributed to accelerated wound closure and epidermal regeneration.

The pathological accumulation of inflammatory chemokines and reactive oxygen species (ROS) establishes a self-sustaining inflammatory feedback loop that critically impedes cutaneous wound healing[70]. Therefore, the anti-inflammatory effects of CSFCM at the gene level were studied by a Quantitative Real-time PCR (qPCR) experiment. Supplementary Fig. 17 depicted the mRNA expression levels of inflammatory cytokines (IL-6, TNF-α, IL-1β) in RAW264.7 cells after 24 h of treatment with Lipopolysaccharides (LPS, 1 μg·mL^{-1}). CSFCM incubation resulted in significantly lower mRNA expression levels of IL-6, TNF-α, and IL-1β compared to the positive LPS group (0.54, 0.58 and 0.22-fold, respectively). In contrast, a modest decrease was noted in the CM and CSF groups due to the presence of anti-inflammatory cytokines in CM (TGFβ) and the anti-inflammatory and antioxidant properties of CS itself[71,72]. As a result, CSFCM combined the anti-inflammatory properties of both and were able to reduce inflammation in LPS-induced inflammatory macrophages. The ROS scavenging activity of CSFCM was also investigated using a fluorescent probe, 2′,7′-dichlorofluorescein diacetate (DCFH-DA). After CSFCM incubation, the fluorescence intensity of RAW 264.7 cells decreased significantly when compared to the LPS positive control (Supplementary Fig. 18), indicating that the associated ROS level was decreased as well. At the same time, CSF also showed some ROS-scavenging ability, which was attributed to the potential anti-inflammatory effect of CS. In general, CSFCM combined the benefits of both CM and CSF, allowing them to effectively lower ROS and inflammatory factors during the inflammatory phase of wound healing, hence promoting the healing process. The CSFCM system demonstrated potent anti-inflammatory activity and enhanced keratinocyte/fibroblast dynamics, establishing a platform for synergistic intervention in complex pathological wound microenvironments.

Spatiotemporal optimization of micromotors in full-thickness cutaneous wound healing in murine models

Our experimental validation confirmed that CSFCM simultaneously enhanced cellular proliferation/migration while suppressing inflammatory responses in vitro. Building upon these findings, we established a murine model of full-thickness skin injury to comprehensively assess the therapeutic efficacy and biological safety of this platform across spatial and temporal healing phases.

We first constructed a murine full-thickness skin defect model. Following anesthesia, 10 mm circular full-thickness wounds were surgically created in depilated dorsal skin regions of BALB/c mice using standardized techniques. To assess the spatial influence of CSFCM + M micromotors on damaged skin tissue, we investigated their active penetration capability using fluorescently labeled micromotors. RhB-CSFCM were prepared by integrating the water-soluble fluorophore during synthesis. A murine full-thickness skin defect model was established, with RhB-CSFCM + M applied to wounds, followed by magnetic field activation (20 min every other day). Non-magnetic controls received identical treatment without field exposure. At day 5 post-intervention, skin tissues were harvested for cryosectioning and fluorescence microscopy. Imaging revealed pronounced deep tissue penetration of RhB-CSFCM + M micromotors under magnetic actuation, evidenced by diffuse red fluorescence throughout granulation tissue (Supplementary Fig. 19). In contrast, non-magnetic controls showed fluorescence localized predominantly at the surface, confirming that magnetic propulsion significantly enhances penetration depth.

By the third postoperative day, wound surfaces typically form a desiccated scab composed of coagulated blood, exudate, and necrotic debris, beneath which healing processes initiate. However, mechanical stressors—including epidermal desiccation, localized tension, and physical abrasion—often compromise the scar itself or the adhesion between scab and tissue, resulting in micro-fissures. We posited that CM-functionalized micromotors leveraged these structural discontinuities to infiltrate sub-scab regions, whereas static microspheres remain surface-bound due to passive diffusion limitations. This dynamic penetration mechanism enables targeted bioactive delivery to regeneration zones, overcoming the spatial constraints imposed by conventional topical therapies.

We further evaluated the therapeutic outcomes of CSFCM + M micromotors in vivo. In brief, the wound was covered with different samples once the wound was formed, which was administered every other day in the first week, and the micromotors group (CSFCM + M) was stimulated by a magnetic field for 20 min. Images were collected every other day for further assessment of the wound area. As shown in Fig. 5A, the wounds treated with micromotors were obviously smaller than other groups. Furthermore, a typical illustration of wound shrinkage and the relative wound closure area at different times systematically demonstrated the wound healing condition (Fig. 5B, C). The results showed that micromotors treatment resulted in a much greater healing rate of the wound area than CSFCM without a magnetic field and other control groups in the later stages of wound healing, with nearly complete healing on day 13. In particular, at day 13, the micromotor treatment resulted in a 52.02% reduction in relative wound area compared to the CSFCM group without a magnetic field. The CSFCM + M group demonstrated significantly accelerated wound closure kinetics relative to non-magnetic CSFCM controls, a therapeutic enhancement driven by magnetically guided deep tissue penetration that optimized bioactive factor delivery to regeneration-critical niches. Notably, the limited efficacy observed in the CM-deficient micromotor group (CSF + M) underscored that propulsion alone was insufficient to drive healing-highlighting the indispensable

https://doi.org/10.1038/s41467-025-61914-8

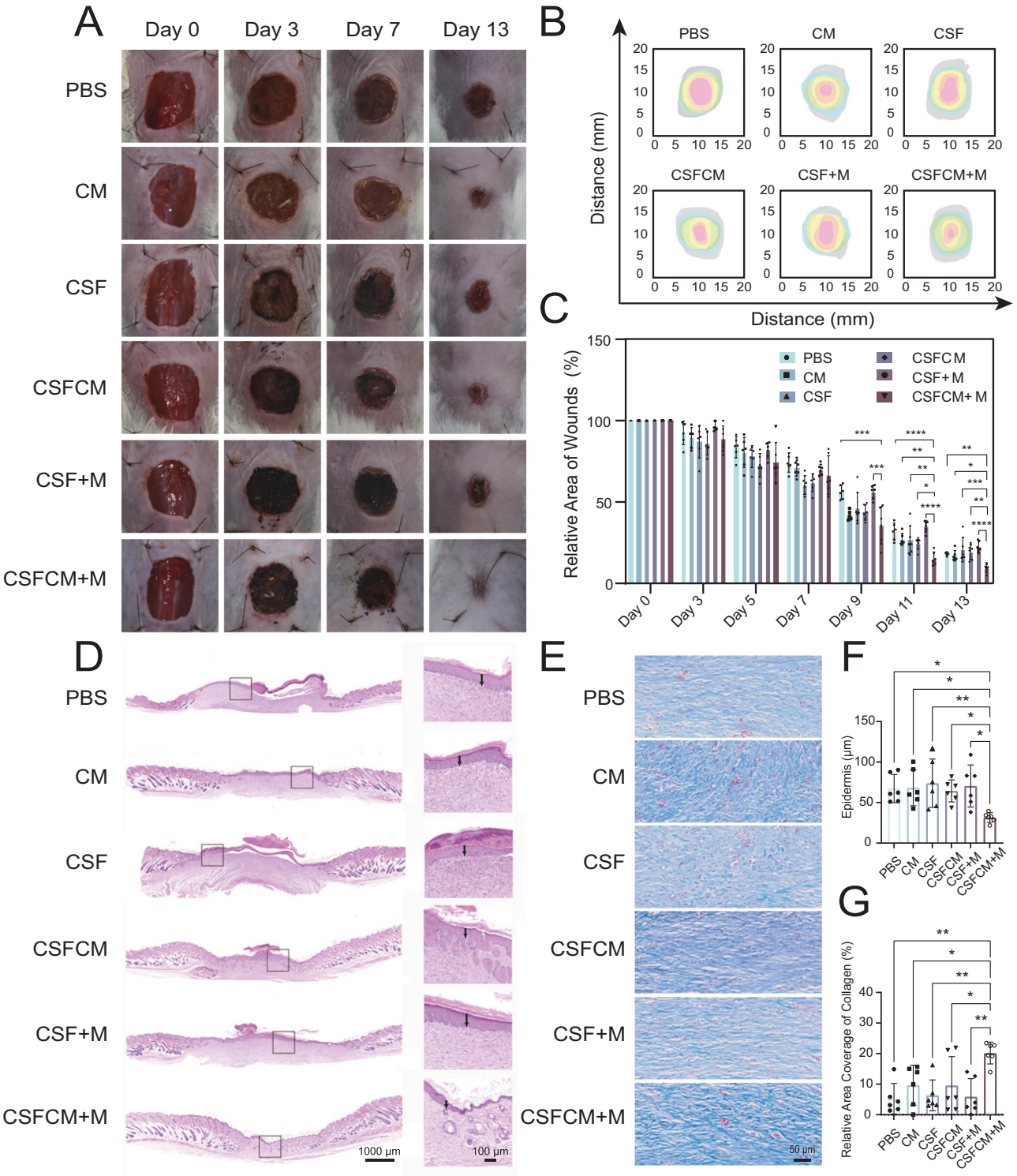

synergy between active delivery and CM's composite bioactivity. This spatiotemporally coordinated strategy ensured sustained therapeutic bioavailability at pathologically relevant depths, circumventing the intrinsic limitations of passive diffusion systems while synchronizing biological interventions with healing phase demands.

Skin repair after injury is generally essential for wound healing, including epithelial re-formation and remodeling, inflammation, and hemostasis. To investigate the spatial and temporal regulation of healing processes by micromotors, skin wound tissues were collected on day 13 post-wounding and the formation of new epithelial was further evaluated by histological examination (HE). The dermal gap length of the wound without appendages can reflect the wound healing, and the micromotors group had the smallest gap as shown in Fig. 5D. The histological results also demonstrated that the epidermal thickness in CSFCM + M group was thinner than all other five groups, which was 51.07% reduction compared to CSFCM group, indicating that the actuated motion behavior of micromotors could advance the formation of wound epidermis (Fig. 5D, F). Moreover, a mature epidermal morphology and hair follicle formation similar to normal skin were also observed in the H&E staining images of the micromotors group (CSFCM + M). These results suggested that the composite active factor micromotor system can promote epithelial re-formation in the

Fig. 5 | CSFCM + M accelerated full skin defect wound healing in mice. **A** Representative general images of the wounds on 3rd, 7th, and 13th day after different treatments. $n = 6$ independent samples. **B** Overlaid images of the wound area during 13 days in different groups. **C** Statistical results of the wound closure ($n = 6$ independent samples). In Fig. 5C, $^{*}p < 0.05$, $^{**}p < 0.01$, $^{***}p < 0.001$, $^{****}p < 0.0001$, for the data in Day 9, the exact P value between CSFCM + M and PBS group was 0.0002, the exact P value between CSFCM + M and CSF + M group was 0.0002; for the data in Day 11, the exact P value between CSFCM + M and CM group was 0.0051, the exact P value between CSFCM + M and CSF group was 0.009, and exact P value between CSFCM + M and CSFCM group was 0.0404; for the data in Day 13, the exact P value between CSFCM + M and PBS group was 0.0078, the exact P value between CSFCM + M and CM group was 0.0331, the exact P value between CSFCM + M and CSF group was 0.0005, and the exact P value between CSFCM + M and CSFCM group was 0.0028. H&E (**D**) and Masson staining (**E**) of the collected skin tissue at day 13 post-wounding. **F** Quantitative data of epidermis thickness for different groups on the 13th day ($n = 6$ independent samples). For the data in Fig. 5F, $^{*}p < 0.05$, $^{**}p < 0.01$, the exact P value between CSFCM + M and PBS group was 0.0232, the exact P value between CSFCM + M and CM group was 0.0185, the exact P value between CSFCM + M and CSF group was 0.0059, the exact P value between CSFCM + M and CSFCM group was 0.0410, the exact P value between CSFCM + M and CSF + M group was 0.0122. **G** Quantitative relative area coverage of collagen ($n = 6$ independent samples). For the data in Fig. 5G, $^{*}p < 0.05$, $^{**}p < 0.01$, the exact P value between CSFCM + M and PBS group was 0.001, the exact P value between CSFCM + M and CM group was 0.0255, the exact P value between CSFCM + M and CSF group was 0.0024, the exact P value between CSFCM + M and CSFCM group was 0.0243, the exact P value between CSFCM + M and CSF + M group was 0.0018. Data in **C, F**, and **G** were presented as mean ± S.D. P values were analyzed by one-way ANOVA with Tukey's multiple comparisons test. Source data are provided as a Source Data file.

wound healing process. As an essential component of skin tissues, the deposition of collagen fibers is the primary marker of tissue remodeling and maturation in the wound healing process. Typically, Masson's staining was used to assess the healing effect of different treatments. As shown in Fig. 5E, compared to other controls, the wounds treated with micromotors exhibited obvious collagen deposition (blue) and had an orderly and uniform arrangement of collagen fibers. Furthermore, the collagen content of wound dermis was calculated and represented by the average optical density using the ImageJ software. There was a significant increase of collagen fibers in CSFCM + M groups and the collagen content of CSFCM + M was 110.39% higher than that of the passive CSFCM group (Fig. 5G). As a result, active CSFCM + M micromotors demonstrated superior therapeutic efficacy in wound healing compared to both control and passive CSFCM groups, achieving spatiotemporally coordinated healing through precision delivery. This multimodal enhancement manifested as accelerated re-epithelialization, organized collagen deposition, and functional restoration of epidermal architecture.

Persistent inflammatory responses at wound sites critically impede healing progression while promoting fibrotic scarring, establishing inflammation modulation as a key determinant of regenerative outcomes. To evaluate CSFCM + M micromotors' anti-inflammatory capacity, we performed histological analyses of key pro-inflammatory mediators IL-6 and TNF-α. After motor treatment, the expression levels of IL-6 and TNF-α were significantly suppressed compared to controls (Figs. 6A, B). Besides, according to statistical analysis, a significant difference was observed between CSFCM + M and the other groups (Fig. 6D and E), while expression levels of IL-6 and TNF-α in CSFCM + M were 82.23% and 85.27% lower than that of CSFCM treatment. Western blot assays were also performed to evaluate IL-6 and TNF-α protein expression levels in skin tissues across all experimental groups. The results demonstrated that the CSFCM + M micromotor group exhibited significantly reduced expression of both IL-6 and TNF-α (Supplementary Fig. 20), consistent with the immunohistochemical findings. This precision cytokine regulation correlated with observed acceleration of healing kinetics and improved tissue repair, confirming the system's synergistic effect in resolving inflammatory dysregulation while promoting structural repair.

Furthermore, angiogenesis is vitally important for tissue regeneration during wound healing, therefore double immunofluorescence staining of CD31 and alpha smooth muscle actin (α-SMA) was carried out to assess the vascularization behavior of the skin tissue. CD31 is a vascular endothelial cell marker and α-SMA is the marker of the vascular smooth muscle cells. It was found that positive staining of CD31 and α-SMA were densely distributed in the CSFCM + M group, whereas little detection was observed in the control group (Fig. 6C). In the CSFCM and CM groups, the vascular structures were present at a moderate level, which was attributed to the vascular endothelial growth factor A (VEGF-A) in CM. By enzyme-linked immunosorbent assay (ELISA), the concentration of VEGF-A in CM was 350.84 ± 8.98 pg·mL^{-1} (CM content is 50 mg·mL^{-1}). Notably, the co-localization pattern of CD31 and α-SMA positive staining was obviously seen in CSFCM+M group, suggesting the formation of mature blood vessel. The semi-quantitative analysis of CD31 and α-SMA was also in line with these results (Fig. 6F, G), with CSFCM + M having 60.44% and 61.31% higher levels of α-SMA and CD31, respectively, than those of CSFCM. These results demonstrated that the micromotors facilitated the maturation of blood vessels in vivo. The aforementioned findings demonstrated that micromotors actively coordinated synergistic intervention requirements within the healing cascade, exhibiting superior therapeutic outcomes in wound closure, anti-inflammatory activity, tissue remodeling, and vascular regeneration compared to control groups. This evidence confirmed the spatiotemporally optimized therapeutic efficacy achieved through synergistic integration of magnetic delivery and bioactive modulation.

We further evaluated the biocompatibility of CSFCM as it relates to clinical translation of therapeutics. The hemolysis assay results demonstrated that both CSF and CSFCM had a negligible hemolysis (< 1.5 %) compared to that of water (100.0 ± 2.85) % (Supplementary Fig. 21), suggesting that the application of CSFCM were feasible and safe. Furthermore, the potential toxicity of CSFCM and CSFCM + M in vivo was also evaluated. As shown in Supplementary Fig. 22, the HE staining imaging of the main organs, including the lungs, heart, spleen, kidneys, and liver, had no obvious histopathological changes in mice after different treatments. Moreover, the serum biochemical results showed that the level of detection indexes (including Alkaline phosphatase (ALP), Alanine aminotransferase (ALT), Aspartate aminotransferase (AST), Urea nitrogen (UREA), Serum Creatinine (CREA-S) and Creatine Kinase (CK) were within the normal range, suggesting that CSFCM and CSFCM + M did not have any hepatic or renal injury (Supplementary Fig. 23). These results highlight the good biocompatibility of CSFCM and CSFCM + M.

Spatiotemporal optimization of micromotors in full-thickness cutaneous wound healing in porcine models

Porcine skin demonstrates critical anatomical and physiological parallels to human tissue, particularly in epidermal structure, dermal appendage patterning, and re-epithelialization driven repair mechanisms. These intrinsic biological similarities establish porcine full-thickness wound models as clinically relevant platforms for evaluating therapeutic interventions. To validate the therapeutic potential of CSFCM + M in porcine models, we isolated BM-MSCs from porcine bone marrow tissues for CM preparation. Using an adherence-based isolation method, primary cells exhibiting characteristic fibroblast-like morphology were successfully cultured from whole bone marrow aspirates. Cell identity was confirmed through comprehensive phenotypic characterization, including flow cytometric analysis of surface

https://doi.org/10.1038/s41467-025-61914-8

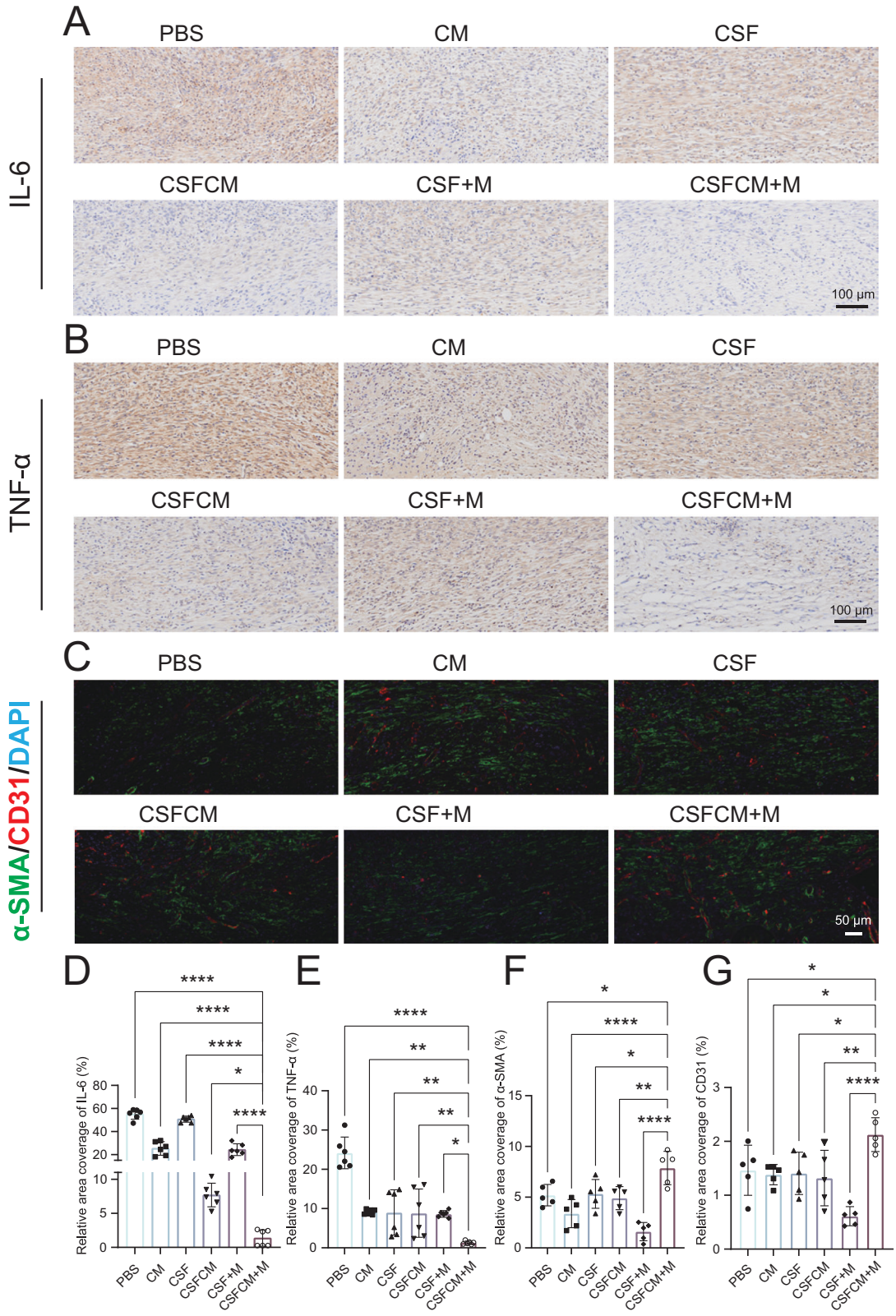

markers and functional validation of multipotent differentiation capacity. Flow cytometry revealed robust expression of MSC-associated markers (CD44: 99.5%, CD90: 99.4%, CD105: 51.8%) with minimal hematopoietic contamination (CD11b: 0.12%) (Supplementary Fig. 24), consistent with established porcine BM-MSC profiles in the literature[73,74]. And the gating strategy was shown in Supplementary Fig. 25. Functional validation through osteogenic and adipogenic differentiation assays demonstrated the cells' multipotency: Osteogenic induction produced mineralized nodules detectable by alizarin red staining. Adipogenic induction generated lipid droplet-containing cells confirmed by oil red O staining (Supplementary Fig. 26). Control groups under non-inductive conditions showed no evidence of mineralization or lipid accumulation, confirming the differentiation specificity of these extracted BM-MSCs. These findings collectively

Fig. 6 | Immunohistochemical and neovascularization analysis of wound tissue in mice. A, B Representative images of immunohistochemistry staining for IL-6 and TNF-α, respectively. $n = 6$ independent samples. **C** Neovascularization in different groups. **D**–**G** Quantified data of the relative area coverage of IL-6, TNF-α, α-SMA, and CD31, respectively. $n = 6$ independent samples in results (**D**) and (**E**), while $n = 5$ independent samples in results (**F**) and (**G**). For the data in Fig. 6D, $^{*}p < 0.05$, $^{****}p < 0.0001$, the exact P value between CSFCM + M and CSFCM group was 0.0356. For the data in Fig. 6E, $^{*}p < 0.05$, $^{**}p < 0.01$, $^{****}p < 0.0001$, the exact P value between CSFCM + M and CM group was 0.006, the exact P value between CSFCM + M and CSF group was 0.0068, the exact P value between CSFCM + M and CSFCM group was 0.0086, the exact P value between CSFCM + M and CSF + M group was 0.0108. For the data in Fig. 6F, $^{*}p < 0.05$, $^{**}p < 0.01$, $^{****}p < 0.0001$, the exact P value between CSFCM + M and PBS group was 0.0128, the exact P value between CSFCM + M and CSF group was 0.0185, and the exact P value between CSFCM + M and CSFCM group was 0.0054. For the data in Fig. 6G, $^{*}p < 0.05$, $^{**}p < 0.01$, $^{****}p < 0.0001$, the exact P value between CSFCM + M and PBS group was 0.0343, the exact P value between CSFCM + M and CM group was 0.0155, the exact P value between CSFCM + M and CSF group was 0.0197, the exact P value between CSFCM + M and CSFCM group was 0.008. Data in **D**–**G** were presented as mean ± S.D. P values were analyzed by one-way ANOVA with Dunnett's multiple comparisons test. Source data are provided as a Source Data file.

verified the successful isolation and characterization of porcine BM-MSCs for subsequent CSFCM production and therapeutic evaluation.

To further evaluate the therapeutic potential of CSFCM + M micromotors in large mammals, a standardized porcine full-thickness skin injury model (20 mm diameter, extending to the fascial layer) was surgically created on the minipig dorsum following preoperative sterilization. Therapeutic interventions were administered every other day for 14 days, with the micromotor-treated group (CSFCM + M) receiving localized magnetic field stimulation (20 min post-administration). Wound healing progression was monitored through serial photographic documentation, using complete re-epithelialization as the primary endpoint. Tissue samples were collected post-healing for histopathological evaluation.

Longitudinal photographic images revealed accelerated wound closure in the micromotor-treated group, with complete wound closure achieved by day 28 compared to control groups (Fig. 7A). Quantitative analyses of relative closure areas and the overlaid images of wound area across multiple time-points further confirmed enhanced healing progression in the micromotor intervention group (Fig. 7B, C). During later-stage healing, the micromotor-treated group exhibited significantly higher closure rates than both non-magnetic CSFCM and CM-only controls, consistent with therapeutic outcomes observed in prior murine full-thickness defect models. Representative histological H&E staining and Masson staining results at day 28 post-wounding showed complete wound closure and significantly smaller granulation tissue area and width in the micromotor-treated group than in the other control groups, suggesting that scar hyperplasia was minimal and collagen reconstruction was more complete in the newly formed tissue following micromotor treatment (Fig. 7D). Histopathological evaluation further confirmed enhanced skin tissue repair and regeneration: H&E staining showed near-complete epidermal regeneration in the micromotor group, with epidermal thickness approximating normal skin levels (28.05% less than CSFCM group; Figs. 7E, G); Masson's trichrome staining further revealed organized collagen architecture in treated wounds, contrasting with disorganized fibrillar patterns in Phosphate Buffered Saline (PBS) controls (Fig. 7F). Collagen density in the micromotor group nearly doubled passive CSFCM levels (91.05% improvement), confirming active tissue remodeling (Fig. 7H).

Therapeutic outcomes demonstrated accelerated wound closure, enhanced re-epithelialization, and structurally mature tissue remodeling (manifested as organized collagen deposition) in the micromotor-treated group compared to non-motorized controls, indicating coordinated spatiotemporal regulation of the healing process. These findings align with prior murine model observations, substantiating CSFCM + M micromotors' dual mechanism of action: (1) magnetic navigation enabling deep tissue penetration and (2) sustained release of bioactive factors promoting proliferative, anti-inflammatory, and remodeling responses. The coordinated biological and physical interventions resulted in structurally mature regeneration, establishing this platform as a promising strategy for complex wound management.

Discussion

We have described a multifunctional micromotor system (CSFCM + M) that integrated bioactive and magnetically propelled properties to address the critical challenge of spatiotemporal regulation in deep wound repair. Engineered through emulsification-crosslinking techniques, CSFCM encapsulated CM within chitosan microspheres, enabling sustained release of therapeutic factors. In vitro evaluations demonstrated CSFCM's dual therapeutic capabilities: temporally coordinating healing processes by enhancing fibroblast/keratinocyte proliferation and migration while suppressing inflammatory cascades, and spatially overcoming physical barriers through magnetically guided penetration of simulated thrombus. In murine full-thickness wound models, CSFCM + M micromotors actively navigated dense scab layers to deliver therapeutics deep into granulation tissue, accelerating healing via synchronized anti-inflammatory, collagen remodeling, and pro-angiogenic effects. Validation in porcine models—anatomically analogous to human skin-confirmed consistent therapeutic outcomes, including accelerated closure, reduced fibrosis, and near-physiological epidermal regeneration with organized collagen architecture. Cross-species efficacy underscored the system's translational potential through synergistic "magnetic propulsion-bioactive modulation" interplay. By converging materials engineering and regenerative biology, this platform transcended static interventions of conventional dressings, establishing a multifunctional therapeutic system encompassing sustained release, targeted delivery, and synergistic interventions regulation, offering a clinically translatable strategy for high-quality tissue repair in complex injuries.

Our study introduced a magnetically actuated chitosan-based micromotor functionalized with MSC secretome, which addressed two critical challenges in regenerative medicine, including the spatiotemporal limitations of therapeutic delivery in deep wounds and the clinical hurdles associated with direct stem cell therapy. For clinical applications, the developed micromotor system provided a cell-free treatment option for replacing stem cells. The advantage of deep tissue penetration was particularly valuable for treating chronic ulcers or burn injuries where topical agents often failed to reach affected hypodermal layers. The long-lasting, slow-release property also improved the bioavailability of the active factor at wound sites. In addition, the flexibility of the modular design allowed for encapsulation/covalent attachment of additional therapeutic payloads (e.g., antibiotics, siRNA), enabling personalized combination therapies tailored to specific wound microbiomes or patient profiles. In a basic research sense, this platform used a modular design to decouple mechanical (magnetic propulsion) from biochemical (secretome) contributions to tissue regeneration. This intelligent CM delivery platform matches the synergistic interventions repair needs of complex wound healing, providing a clinically tractable solution for spatiotemporally controlled wound intervention.

Methods

Materials

Chitosan (Mw 50 kDa) with 90% degree of deacetylation (DDA), paraffin liquid, Tween 80, Span 80, petroleum ether, isopropyl alcohol, Poly (4-styrenesulfonic acid-co-maleic acid) sodium salt (PSSMA, Mw ≈ 20000, SS: MA = 1: 1), ethylene glycol, ferric chloride hexahydrate ($FeCl_3{\cdot}6H_2O$), sodium acetate (NaAc, ≥99.0%), sodium hydroxide

https://doi.org/10.1038/s41467-025-61914-8

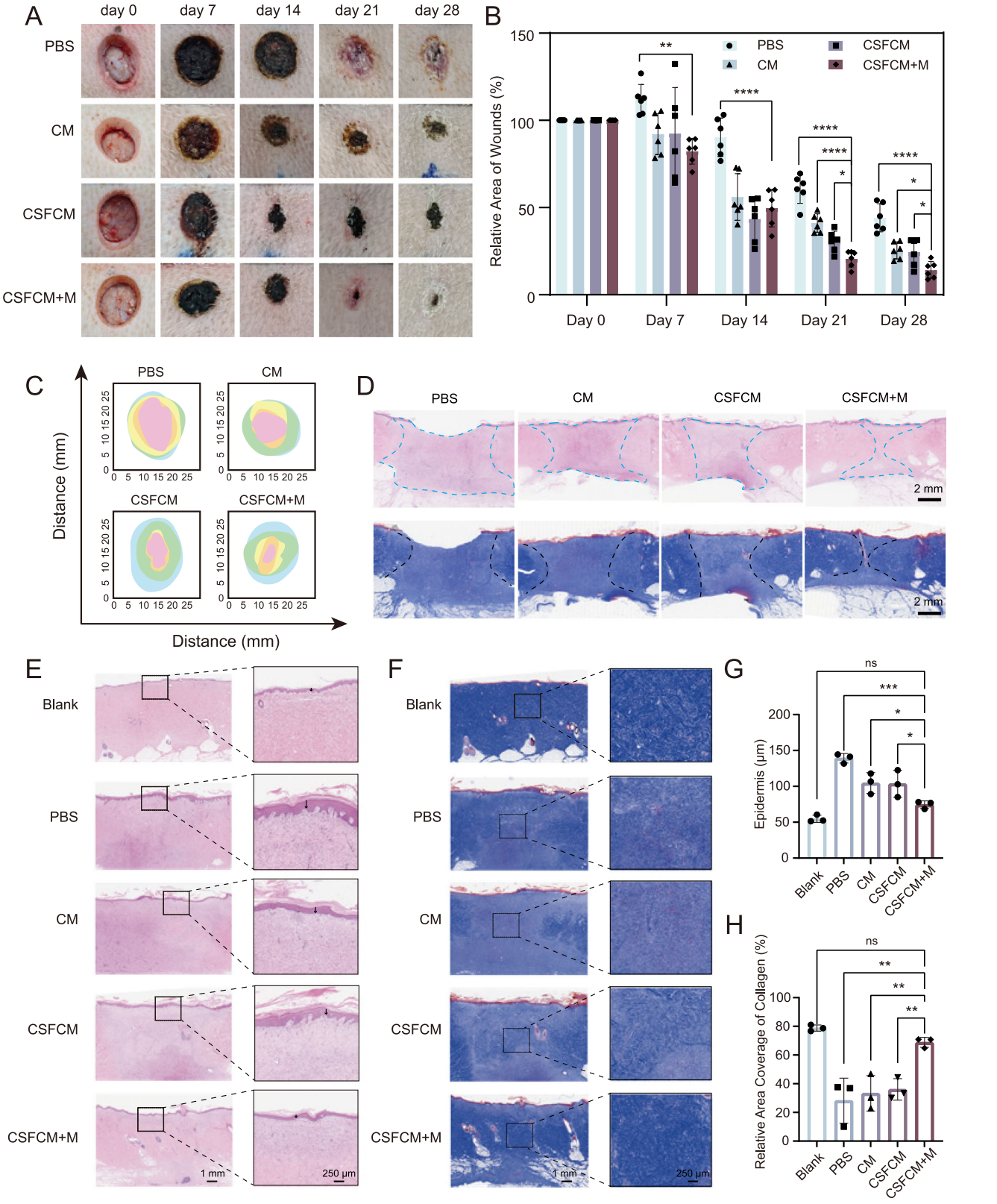

(NaOH, ≥99.0%), potassium hydroxide (KOH, ≥99.0%) were all purchased from Sigma Aldrich. Unless otherwise specified, the chemicals used in this work were all bought from Sigma-Aldrich. Ethylene glycol was pre-dried by enough molecular sieve (type 3 A) while other reagents were used as received without further purification. All reagents for cell culture were bought from Gibco. The purified deionized water was prepared by the Milli-Q plus system (Millipore, USA).

Cell lines and animals

Human Keratinocytes Cells (HaCaT cells, AW-CH0096) were purchased from AnWei-Sci., Mouse Embryonic Fibroblast Cells (NIH/3T3 cells) were kindly provided by Dr. Weichang Huang from the First Clinical Medical College of Southern Medical University, and Mouse Mononuclear Macrophages Cells (RAW 264.7 cells, CL-0190) were purchased from Wuhan Pricella Biotechnology Co., Ltd., which

Fig. 7 | CSFCM + M accelerated wound healing in full-thickness porcine skin wound model. A Representative images of wounds after different treatments at different time points. $n = 6$ independent samples. **B** Statistical results of relative wound area ($n = 6$ independent samples). In Fig. 7B, $^{*}p < 0.05$, $^{**}p < 0.01$, $^{****}p < 0.0001$, for the data in Day 7, the exact P value between CSFCM + M and PBS group was 0.0092; for the data in Day 21, the exact P value between CSFCM + M and CSFCM group was 0.0326; for the data in Day 28, the exact P value between CSFCM + M and CM group was 0.0221, and the exact P value between CSFCM + M and CSFCM group was 0.0359. **C** Overlaid images of the wound area in different treatment groups over 28 days. **D** Comparison of granulation tissue area and width of skin tissue in different treatment groups. Plots of H&E and Masson staining results of skin tissues and their local magnification. **E** Epidermal thickness of different treatment groups. **F** collagen deposition amount of different treatment groups. Statistical results of epidermal thickness (**G**) and collagen deposition (**H**) in skin tissues of different treatment groups ($n = 3$ independent samples). For the data in Fig. 7G, $^{*}p < 0.05$, $^{***}p < 0.001$, the exact P value between CSFCM + M and PBS group was 0.0002, the exact P value between CSFCM + M and CM group was 0.029, the exact P value between CSFCM + M and CSFCM group was 0.0352. For the data in Fig. 7H, $^{**}p < 0.01$, the exact P value between CSFCM + M and PBS group was 0.0015, the exact P value between CSFCM + M and CM group was 0.0040, the exact P value between CSFCM + M and CSFCM group was 0.0067. Data in **B**, **G**, **H** were presented as mean ± S.D. P values were analyzed by one-way ANOVA with Dunnett's multiple comparisons test. Source data are provided as a Source Data file.

were cultured in high glucose DMEM complete medium (Procell, PM150210B). Mouse-derived BM-MSCs were isolated from male Balb/c mice (3-4 weeks old, 12 ~ 16 g), and porcine-derived BM-MSCs were isolated from male Bama miniature pig (9 months old, 25-35 kg), which were cultured in MEM Alpha basic medium (α-MEM, C12571500BT, Gibco) supplemented with 10% FBS (Gibco) and 1% penicillin-streptomycin (Gibco). The cells were cultured in a 5% CO_2 humidified incubator at 37 °C. Male Balb/c mice (3-4 weeks old, 12 ~ 16 g) and male Balb/c mice (6-7 weeks old, 18 ~ 22 g) were purchased from Southern Medical University Experimental Animal Center. The mice had access to food and water ad libitum and were hosted in ambient temperature (21–26 °C), humidity at 50-60%, under 12 h dark/light cycles. Male Bama miniature pig (9 months old, 25-35 kg) were purchased from Guangdong Bright Pearl Biotechnology Co., LTD. Small pigs were housed in single cages, the ambient temperature of the animal room was 18-22 °C, the daily temperature difference was not more than 4 °C, the relative humidity was 40-70%, and 12 h of lighting/12 h of darkness were alternated between light and darkness. All animal experiments were approved by the Institutional Animal Care and Use Committee of Southern Medical University (Protocol Registry Number: SMUL202311047 and SMUL202409046) and followed all aspects of the institutional guidelines.

Instruments

The structures of the formed microspheres were analyzed with transmission electron microscope (TEM, Talos L120C, Thermofisher) with an acceleration voltage of 120 kV. Scanning electron microscope (SEM) images and Energy-dispersive X-ray spectroscopy (EDX) elemental mappings were recorded on a Phenom emission scanning electron microscope (PhenomProX, Phenom) with an accelerating voltage of 15 kV. Zeta potential were performed on Zetasizer Nano ZSE (Malvern, UK) with 25 °C and 633 nm He-Ne laser wavelength. The crystal structure of magnetic chitosan microspheres was determined by X-ray powder diffractometer (XRD, D8 Advance, Bruker) with a scan rate of $10°{\cdot}min^{-1}$ and the 2θ range of 5–90°. The hysteresis curve of the micromotors was determined by vibrating sample magnetometry (VSM, LakeShore 7404) with the parameters set to room temperature and a magnetic field range of −20,000 to 20,000 Oe. The morphology of the samples, cell staining images and micromotor's motion video were captured on an inverted fluorescence microscope (Ti2-A, Nikon, Japan). The penetration situation of the micromotors in the simulated thrombus was recorded in an inverted laser confocal microscope (FV3000, Olympus). The UV-vis absorption was measured with a microplate reader (Biotek 800 TS, USA). The fluorescent quantitation reverse transcription of qPCR was conducted in a Roche 480 fluorescence quantitative PCR instrument (LightCycler® 480, Roche). Protein signals were visualized using a chemiluminescence detection system (TANON-5200 M). All the stained histological sections were observed with an Olympus VS200 whole slide imaging system (Olympus, Japan). The blood samples were tested by fully Automatic Biochemical Analyzer (BS-330E, mindray, China).

Mouse derived BM-MSCs isolated and cultured

Three Balb/c mice (male, 3-4 weeks old) were sacrificed by cervical dislocation and soaked in 75% (V/V) ethanol for 10 min with the whole body in a 250 mL beaker. The mice were then transferred to an operating table, where the femurs and tibiae were separated along the skin incision by using surgical scissors. The adherent skin and muscles were carefully disassociated from the bones and washed twice with PBS supplemented with 2% penicillin/streptomycin (100 $U{\cdot}mL^{-1}$ and 100 $\mu g{\cdot}mL^{-1}$; Gibco, Thermo Fisher Scientific). The bones were then transferred onto sterile gauze for further cleaning of the residual soft tissues and BM-MSCs were harvested by flushing with PBS supplemented with 2% heat-inactivated FBS until the bones became pale. Next, BM-MSCs were transferred to a new 100 mm sterile culture dish with 10 mL complete α-MEM medium and incubated at 37 °C in a 5% CO_2 incubator. After initial bone marrow cell plating, we removed supernatant at 3 h to eliminate non-adherent hematopoietic populations, followed by a deliberate reduction in medium disturbance until day 3. Partial or full medium replacement was then conducted on day 3 based on visual adherence assessments, and again completely replaced on day 5. Cell harvesting occurred at 70-90% confluence using 0.25% trypsin, with digestion durations strictly capped at 2 min to preserve viability. This phased approach aimed to mitigate HSC contamination while permitting murine BM-MSCs to retain functional niche interactions critical for their survival and proliferation.

Flow cytometry identification of mouse BM-MSCs

The mouse-derived cultured BM-MSCs at passage 3 were collected by trypsin digestion and washed twice with PBS buffers containing 1% FBS. Cells aliquots ($1{\times}10^5$) were stained with APC/Cy7-CD44 (Biolegend, 103028, 1:200), APC-CD90 (Elabscience, E-AB-F1283E, 5 μL/Test), PE/Cy7-Sca-1(Biolegend, 108113, 1:200), PE-CD105(Biolegend, 120407, 1:200), FITC-CD45 (Elabscience, E-AB-F1136C, 5 μL/Test), APC-CD34 (Biolegend, 152216, 1:200) with 30 min, and further analyzed using a BD flow cytometer and Flowjo software (Flowjo_V10).

Porcine derived BM-MSCs isolated and cultured

Porcine BM-MSCs were isolated through a modified classical whole marrow protocol. Following euthanasia, femoral and tibial bones were excised from a male Bama miniature pig (9 months old, 25-35 kg) with residual muscle tissue surgically removed under aseptic conditions. The bones underwent sequential disinfection in 75% ethanol, followed by triple PBS rinses containing antimicrobial agents to eliminate biological contaminants. Marrow cavities were exposed by removing epiphyseal ends, then flushed with basal medium using sterile syringes until complete cellular extraction. The collected marrow suspension was centrifuged to pellet nucleated cells, which were subsequently resuspended in complete culture medium supplemented with FBS. Primary cultures were established in tissue-treated flasks, with initial medium replacement after 3 h to remove non-adherent cells. Cultures were maintained under standard

conditions with periodic medium changes (2-3 days) until reaching 80-90% confluence. Subculturing was performed via brief enzymatic dissociation (2 min), with cells passaged at appropriate expansion ratios (1:2) to maintain proliferative capacity.

Flow cytometry identification of porcine-derived BM-MSCs

Porcine BM-MSCs at passage 3 were analyzed for surface marker expression via flow cytometry. Upon reaching 80–90% confluence, adherent cells were detached using enzymatic treatment for 2 min, washed, and centrifuged to obtain single-cell suspensions. Cells were sequentially incubated with biotinylated primary antibodies targeting CD105 (Biotin-CD105, Thermo, MA5-28545, 1:200) for 1 h, followed by PE Streptavidin (Biolegend, 405203, 1:300), PE/Cy7-CD44 (Biolegend, 103029, 1:200), APC-CD11b (Biolegend, 301309, 5 μL/Test) and APC/Cy7-CD90 (Biolegend, 328131, 5 μL/Test) antibodies for a further 30 min. All staining procedures were conducted under light-protected conditions to preserve fluorophore integrity. Following final washes, labeled cells were resuspended in buffer and analyzed using a BD flow cytometer and Flowjo software (Flowjo_V10) to quantify mesenchymal marker expression profiles.

Validation of the multidirectional differentiation potential of mouse/porcine-derived BM-MSCs

We validated the multidirectional differentiation of BMSCs using an osteogenic/lipogenic induced differentiation kit (OriCell, MUXMX-90021 and MUXMX-90031 for mouse-derived BM-MSCs, GUXMX-90021 and GUXMX-90031 for porcine-derived BM-MSCs).

Identification of osteogenic differentiation induction. The cell culture plate was pre-coated with 0.1% gelatin for 30 min, and the extracted BM-MSCs cells were then cultured. When the cell fusion reached about 70%, the osteogenic differentiation induction medium (OriCell, GUXMX-90021) was added, changed every three days, and continued for 3 weeks. The induction could be stopped when more osteogenic nodules appeared in the cells. After induction, the cells were fixed with 4% paraformaldehyde solution, stained with alizarin red and observed under an inverted fluorescence microscope.

Identification of lipidogenic differentiation induction. Pre-coat the cell culture plate with 0.1% gelatin for 30 min and inoculate the extracted BM-MSCs cells subsequently. When the cell fusion reached about 90%, the lipidogenic differentiation induction medium A solution (containing cell basal medium, FBS, and bone marrow MSC lipid-induced differentiation additives A-I and A-II) was added. After 3 days of induction, the A solution was discarded and replaced with lipid differentiation induction medium B (containing cell base medium, FBS, and bone marrow MSC lipid-induced differentiation additive B). After one day of induction, the B solution was discarded and replaced with the A solution to continue induction, and the A solution and B solution were used alternately until a sufficient number of lipid droplets of appropriate size appeared on the cells, then the induction could be stopped. At the end of differentiation induction, the cells were fixed in 4% paraformaldehyde solution and stained with oil red O. The lipid staining was observed under an inverted fluorescence microscope.

Conditioned medium collection and lyophilization

Mouse/porcine-derived BM-MSCs were sub-cultured to passage 3 for CM collecting. BM-MSCs (2×10^6 cells) at passage 3 were seeded on a 100 mm dish and cultured until 90% confluence, and the medium was then replaced by 10 mL serum-free α-MEM for another 2 days incubation. After 48 h, the supernatant of BM-MSCs was harvested and centrifuged at 300 × *g* for 10 min to remove the dead cells and debris. Besides, the supernatant was filtered by a 0.22 μm filter and then collected for freeze-drying to obtain BM-MSCs derived CM.

Synthesis of magnetite nanoparticles (F)

F were synthesized by an atmospheric solvent-thermal method based on previous reports with slight modifications. Typically, 0.65 g $FeCl_3$ was added into a 100 mL beaker and 40 mL ethylene glycol predehydrated with 3 A molecular sieve was quickly added. Next, 3.0 g NaAc, 1.0 g PSSMA, ascorbic acid (Vc) and an appropriate amount of H_2O were sequentially added. Then sealed with plastic wrap and stirring to obtain a homogeneous mixture. Afterwards, 0.6 g NaOH was added under stirring. Finally, the as-received solution was transferred to a conical bottle and heated in an oven to 190 °C for 9 h. After cooling to room temperature, the black product was collected by centrifugation and washed alternately with 50% ethanol (ethanol:water = 1:1) and deionized water for three times. Then, the product was dispersed in 30 mL distilled water and stored at 4 °C for further usage.

Preparation of magnetic chitosan microspheres (CSF)

CSF were prepared by an emulsion crosslinking method with genipin as crosslinking agent. In a typical procedure, 30 mL liquid paraffin was used as oil phase, 0.9 mL Span 80 was added as emulsifier and 0.09 mL Tween 80 as co-emulsifier. A certain amount of chitosan was dissolved in 1% acetic acid to obtain 1.5% wt chitosan solution, and 3 mL of this solution containing 5 mg F was added to the above oil phase solution under stirring. The water-in-oil (w/o) emulsion was obtained after 1 h, and 2 mL genipin (1% wt genipin dissolved in 50% ethanol solution; V/V, ethanol: water = 1:1) was then slowly dropped into the emulsion at 42 °C. After 4.5 h of crosslinking, the reaction was stopped and chitosan microspheres were obtained by centrifugation at 4020 × *g* for 5 min, washed alternately with petroleum ether, isopropyl alcohol and water, and then stored at 4 °C. The CM loaded microspheres (CSFCM) were prepared by the direct encapsulation method. Briefly, CM with a concentration of 25 mg·mL^{-1} was added into the chitosan solution before emulsification, then, the CSFCM was prepared as described above.

In vitro release

10 mg CSF and CSFCM were dispersed in 1.5 mL PBS (pH 7.4) with 1% (V/V) penicillin/streptomycin, respectively. The mixture was then stirred at 1000 rpm using a ThermoMixer (MIULAB, MTC-100, Hangzhou, China) at 37 °C. At appropriate times, aliquot samples (each 0.7 mL) were withdrawn by centrifuge, and the fresh media (each 0.7 mL) were added immediately after sampling. Each sample was measured with an Enhanced BCA Protein Assay Kit (Beyotime, China) to determine the amount of released CM.

Encapsulation efficiency determination

Briefly, following the preparation of CSFCM, the suspension was centrifuged to separate the CSFCM particles from the supernatant. The supernatant was carefully collected, and a precise volume was used to quantify the amount of free CM that remained unencapsulated. Furthermore, an equivalent volume of the initial oil-water two-phase mixture containing CM (prior to CSFCM preparation) was analyzed to determine the total amount of CM present in the system.

The concentration of CM in both the supernatant (free CM) and the initial mixture (total CM) was measured using a BCA Protein Assay Kit (Beyotime, China), following the manufacturer's instructions. The absorbance was measured at 562 nm using a microplate reader, and the CM concentration was calculated based on a standard curve.

The encapsulation efficiency (EE) of CM in CSFCM was calculated using the following equation:

$$EE(\%) = (C_{total} - C_{free})/C_{total} \times 100\%$$

Where C_{total} represents the total CM concentration in the initial mixture, and C_{free} denotes the concentration of free CM in the supernatant.

Loading capacity determination

To evaluate the loading efficiency of CM within the CSFCM, 10 mg of CSFCM were added in 1.5 mL of 2% acetic acid solution. The mixture was incubated at 37 °C for 24 h to facilitate the complete extraction of CM from the microspheres. Following incubation, the solution was centrifuged to obtain the supernatant, which contained the extracted CM. The CM concentration in the supernatant was quantitatively analyzed using BCA Protein Assay Kit (Beyotime, China), following the manufacturer's protocol.

The loading capacity of CM in CSFCM was calculated using the following equation: Loading Capacity (%) = $m/m_0 \times 100\%$

Where m_0 represents the total mass of CSFCM, and m denotes the mass of CM loaded within the CSFCM.

Cytotoxicity assay

The biocompatibility of CSF and CSFCM was evaluated by assessing their ability to support the growth of NIH/3T3 fibroblasts and HaCaT cells. Cell Counting Kit-8 (CCK-8, Solarbio, Beijing, China) assay was conducted to assess the cytotoxicity of CSF and CSFCM. The cells were seeded (1×10^4 cells/well) into 96-well plate with 200 µL of culture medium and incubated overnight at 37 °C in 5% CO_2. CSF and CSFCM equivalent to the concentration of 0–2000 µg/mL were added to the respective wells and incubation continued for 24 h. After incubation, the original medium was removed gently and 100 µL of CCK-8 solution (V/V, CCK8: DMEM medium = 1:10) was added to each well and incubated for another 2 h at 37 °C. After that, the absorbance value at 450 nm was measured in a microplate reader.

The cell viability was calculated as follows:

$$\text{Cell Viability}(\%) = (OD_{\text{treatment}} - OD_{\text{blank}})/(OD_{\text{control}} - OD_{\text{blank}}) \times 100\%$$

Cell proliferation

HaCaT and NIH/3T3 cells were trypsinized while 80–90% confluence, and the cells were seeded in 96-well plates with a density of 8000 cells per well. After incubation overnight, the cells were treated with base medium (negative control group), complete medium (positive control group), CM (50 µg·mL^{-1}), CSF (100 µg·mL^{-1}), and CSFCM (100 µg·mL^{-1}) respectively, and incubated at 37°C with 5% CO_2 for 24, 48 and 72 h. Experimental treatment solutions were prepared by dispersing respective test compounds in serum-free basal medium across all experimental groups, which can eliminate potential confounding effects from serum-derived growth factors. The cell viability was measured by CCK-8 method at different time points. Briefly, the cells were cultured with 10% CCK-8 solution (Solarbio, Beijing, China) and incubated for 1.5 h at 37 °C in 5% CO_2. The corresponding absorbance value at a wavelength of 450 nm was measured in microplate reader.

$$\text{Proliferation Rate}(\%) = (OD_{\text{time point}} - OD_{\text{blank}})/(OD_{\text{initial time}} - OD_{\text{blank}}) \times 100\%$$

Cell migration

The migration of NIH/3T3 and HaCaT cells was evaluated using a scratch assay method. The cells were digested after the cell fusion reached 90% and seeded in 6-well cell culture plates with a density of 3×10^4 per well. The cells were cultured in DMEM medium containing 10% FBS until the cells fused into a single layer. Then, a pipette tip was utilized to generate a linear scratch wound and the cell debris was rinsed gently with sterile PBS buffer. The scratched cells were then cultured with serum-free basal DMEM medium containing different samples for 24, 48, and 72 h (Control (basic medium), CM (50 µg·mL^{-1}), CSF (100 µg·mL^{-1}), and CSFCM (100 µg·mL^{-1}) respectively. Utilizing serum-free base medium as a dispersing solvent was to eliminate potential confounding effects of serum and to highlight the influence of each test compounds on cell migration. The scratch area was filmed by an inverted fluorescent microscope every 24 h, and the cell migration rate was analyzed using ImageJ Pro Plus software.

Quantitative real-time PCR assay

To further verify the anti-inflammatory ability of CSFCM, we carried out qPCR detection on inflammatory macrophages. In brief, RAW 264.7 cells were plated onto 6-well plates with a density of 3×10^4 cells/well for 12 h. The cells were treated with DMEM basic medium (control group), 1 µg·mL^{-1} LPS (positive control group) and different samples containing LPS (1 µg·mL^{-1}). After 24 h incubation, total RNA of the cells was extracted with RNA extraction kit (Foregene, Chengdu, China) according to the manufacturer's protocol. Next, the first-strand cDNA was synthesized with 500 ng of total RNA using SuperScript II (Yeasen, Shanghai, China). SYBR Green I dye (Yeasen, Shanghai, China) was used for fluorescent quantitation reverse transcription in a Roche 480 fluorescence quantitative PCR instrument following the recommended protocol. The primers of TNF-α, IL-6, IL-1β, and 18S were listed in Supplementary Table 1. All reactions were performed in triplicate, and the data were analyzed using the $2^{-\Delta\Delta Ct}$ method.

Intracellular ROS determination

RAW264.7 cells were seeded in 6-well plates and cultured overnight, and the cells were treated with LPS (1 µg·mL^{-1}), culture medium, LPS plus CSF (100 µg·mL^{-1}), LPS plus CM (50 µg·mL^{-1}) and LPS plus CSFCM (100 µg·mL^{-1}) for 12 h. After incubation, the cells were washed with PBS and incubated with 2′, 7′-dichlorofluorescein diacetate (DCFH-DA) solution (Beyotime, Shanghai, China) for another 30 min. After incubation, the cells were washed with PBS and observed by inverted fluorescence microscope.

Micromotors penetration of simulated thrombus

To examine the ability of micromotors to penetrate deep into thrombus, we studied the response of CSFCM toward the magnetic guidance in an in vitro blood clot. Red blood cells and fibrin were used to simulate blood clots. Briefly, whole mouse blood mixed with DIO dye, 5U thrombin, and 5 mM $CaCl_2$ were added to a confocal dish and shaken at 37 °C for 3 h. The blood clot was then allowed to stabilize at 4 °C. After that, the produced thrombus was treated with 1 mg·mL^{-1} of RhB-CSFCM, and it was magnetically stimulated for 20 min. The control group was the one that did not have a magnetic stimulation under the identical circumstances. The penetration situation was photographed by a FV3000 confocal microscope and further analyzed by Imaris 8.1 software.

Skin wound healing experiments in mouse wound model

To evaluate the ability of CSFCM + M micromotors to promote wound healing, a mouse full-thickness dermal wound model was utilized to validate the ability of micromotors to repair wounds. Thirty-six specific pathogen-free (SPF) grade Balb/c male mice (6-7 weeks old) were purchased from the Southern Medical University Experimental Animal Center. Before the experiment, the mice were raised in the laboratory for one week to adapt to the environment. The mice were then divided into six groups: control, CM, CSF, CSFCM, CSF + M, and CSFCM + M. On the day of the experiment and surgery, the mice were anesthetized by intraperitoneal injection of pentobarbital. After that, shaved the backs of the mice and cleaned them with a depilated cream. Then, disinfect the shaved area with alcohol. Next, we marked the mice on the backs with 10 mm skin punch, and then utilized sterile surgical scissors to cut the full-thickness skin following the circular lines. Finally, the samples of each group were applied to the wound. The wounds treated with different groups were photographed at 0, 1, 3, 5, 7, 9, 11, and 13 days. The wound area was then analyzed with ImageJ software. On the 13th day, all the mice were sacrificed and the skin tissues at the wound site were sliced, followed by H&E staining, Masson-trichrome staining, immunohistochemistry of TNF-α and IL-6, and immunofluorescence staining of CD31 and α-SMA.

Evaluation of the ability of the micromotors to penetrate deep into the skin tissue

The deep tissue penetration capability of CSFCM + M micromotors was evaluated in a murine full-thickness skin defect model. RhB-CSFCM + M micromotors were topically applied to wound beds, followed by localized magnetic field activation (20 min per session, administered every other day). At day 5 post-treatment, animals were euthanized, and skin tissues surrounding the wound sites were harvested for cryosectioning frozen slicer (Leica CM1860 UV) and fluorescence microscopy analysis (inverted fluorescence microscope). Comparative assessments were conducted using non-magnetic controls to isolate the contribution of magnetic propulsion to tissue penetration.

Western blot analysis for protein level detection

Protein expression analysis in skin tissues was performed through standardized western blot protocols. Fresh tissue samples (~ 100 mg) were homogenized in pre-chilled radio immunoprecipitation assay (RIPA) lysis buffer containing protease inhibitors using cryogenic mechanical disruption (70 Hz, on 60 s, off 20 s). Following centrifugation at 14,000 × *g* for 20 min at 4 °C, supernatants were collected for protein quantification via BCA assay. Equalized protein samples were denatured in loading buffer, electrophoresed on polyacrylamide gels, and transferred to PVDF membranes. Membranes were blocked with commercial blocking buffer prior to sequential incubation with primary antibodies (β-actin, Servicebio, GB15001-100, 1: 2500), TNF-α (Proteintech, 60291-1-Ig, 1:2000), IL-6 (Proteintech, 26404-1-AP, 1:1000) and Horseradish Peroxidase (HRP)-conjugated secondary antibodies (Proteintech, SA00001-1 and SA00001-2, 1:8000). After thorough washing, protein signals were visualized using a chemiluminescence detection system. Antibody dilutions and incubation conditions followed manufacturer's recommendations to ensure specificity and reproducibility.

Construction of a porcine full-thickness skin defect model

Preoperative protocols included fasting experimental minipigs (Male Bama miniature pig, 9 months old, 25-35 kg) for 12 h with ad libitum water access. Anesthetic management commenced with intramuscular administration of atropine sulfate (0.05 mg·kg^{-1}) as preanesthetic medication, followed 15 min later by a combination of Zoletil 50 and xylazine hydrochloride for induction. Following induction, animals were positioned in ventral recumbency on the surgical platform, intubated, and maintained under isoflurane anesthesia via a veterinary anesthesia machine (Veta 5, Mindray, China). Continuous physiological monitoring (oxygen saturation, heart rate, blood pressure) was carried out through the patient monitor (ePM12MVet, Mindray, China) to ensured intraoperative stability, with proper airway alignment maintained throughout the procedure.

The dorsal surgical field was prepared through sequential PBS cleansing and alcohol disinfection. After mechanical hair removal using clippers and depilatory cream, six full-thickness circular wounds (2 cm diameter, 4 cm inter-wound spacing) were surgically created paravertebrally using sterile biopsy punches. Each wound extended through the dermal layer to expose the underlying fascia, followed by meticulous hemostasis via pressure and sterile gauze application. Wound beds were irrigated with gentamicin-supplemented saline solution prior to therapeutic intervention.

Postoperative care comprised three-day courses of prophylactic penicillin injections and meloxicam analgesia (0.3 mg·kg^{-1}). Animals were housed individually with daily clinical monitoring to assess recovery status and wound progression.

Skin wound healing experiments in minipig wound model

The therapeutic efficacy of CSFCM + M micromotors was evaluated in porcine full-thickness skin defect model. Following surgical wound creation, animals were randomly assigned to four treatment groups: PBS (negative control), CM (conditioned medium control), CSFCM (non-micromotor control), and CSFCM + M (micromotor with magnetic activation). Therapeutic interventions were administered every other day over a 14-day period. Prior to each treatment session, animals were anesthetized, and sample solutions were topically applied to wound beds. The CSFCM + M group received additional localized magnetic field exposure (20 min post-application) to activate micromotor propulsion. All wounds were subsequently covered with sterile petrolatum gauze and secured with bandages for protection.

Wound healing progression was monitored through serial photographic documentation, with complete re-epithelialization serving as the primary endpoint. On day 28, animals underwent terminal blood collection via cardiac puncture followed by euthanasia. Full-thickness skin samples surrounding healed wounds were bisected longitudinally: one half preserved at -80 °C for future use, the other fixed in 4% paraformaldehyde for histopathological evaluation. The skin tissue sample underwent standard H&E and Masson's trichrome staining to assess epidermal regeneration and collagen deposition patterns.

Histology and immunohistochemistry evaluation

The mice were sacrificed at day 13 post-wounding, and the wound sites containing surrounding skin were as excised. The skin samples were fixed in 4% paraformaldehyde, dehydrated in ethanol and embedded in paraffin, followed by microtome slicing. The skin tissues were sectioned into 4 μm-thick slices for H&E staining, Masson-trichrome staining, immunohistochemistry, and immunofluorescence staining. Immunohistochemical staining of IL-6 (Servicebio, GB11117, 1:200), TNF-α (Boster, BA0131, 1:200), and HRP-conjugated secondary antibodies (SeraCare, 5220-0336, 1:500) were utilized to examine the inflammation response. CD31 (Abcam, ab182981, 1:1000), α-SMA (Boster, BM0002, 1:500) and HRP-conjugated secondary antibodies (SeraCare, 5220-0336 and 5220 0341, 1:400) immunofluorescence staining was used to analyze the neovascularization in wounds. All the stained histological sections were observed with an Olympus VS200 whole slide imaging system (Olympus, Japan). The semi-quantitative analysis of dye markers was assessed by using ImageJ software. At least 3 random areas were selected, and the results were averaged.

Hemolysis assay

Mouse venous whole blood was centrifuged at 4 °C (860 × *g* for 15 min) to collect the precipitate. The precipitate was washed repeatedly with saline (centrifugation at 860 × *g* for 3 min each time), and the erythrocyte suspension was obtained. The concentration of erythrocytes was adjusted to 2% by adding an appropriate amount of erythrocyte suspension to different concentrations of CSF and CSFCM (100, 200, 400 μg·mL^{-1}). Erythrocytes dispersed in saline were used as a negative control group, and those dispersed in deionized water were used as a positive control group. Each condition was performed three times in parallel. The above solutions were mixed and incubated at 37 °C for 3 h, then centrifuged at 860 × *g* for 3 min. Observe the color change of the supernatant and take photographs. The absorbance of the supernatant was measured. The hemolysis rate was calculated according to the following formula:

Hemolysis Rate (%) = (sample absorbance-negative control absorbance)/(positive control absorbance-negative control absorbance) × 100%.

Blood biochemistry

Freshly collected whole blood of the mice was placed in blood collection tubes containing sodium heparin, quickly inverted and mixed, and then centrifuged at 860 × *g* for 15 min at 4 °C. The supernatant was collected, and then the liver function indexes were measured by an automatic biochemistry analyzer: Alanine aminotransferase (ALT), Aspartate aminotransferase (AST), alkaline phosphatase (ALP), renal function indicators: Urea nitrogen (UREA) and Creatinine (CREA), and myocardial injury indicators: Creatine Kinase (CK).

Statistical analysis

Every experiment was conducted in triplicate or more. The experimental data were presented as the mean value with standard deviation (mean ± S.D.) and were analyzed with GraphPad Prism 9.0 (GraphPad Software Inc., La Jolla, CA, USA). Statistical analysis in multiple comparisons were conducted using one-way ANOVA with Tukey's multiple comparisons or one-way ANOVA with Dunnett's multiple comparisons test. $p < 0.05$ was deemed indicative of a statistically significant distinction between the two groups.

Reporting summary

Further information on research design is available in the Nature Portfolio Reporting Summary linked to this article.

Data availability

The source data generated in this study are provided in the Supplementary Information/Source Data file. Source data is available in the associated Figshare dataset: https://doi.org/10.6084/m9.figshare.28786769. Any additional raw data will be available from the corresponding author upon reasonable request. Source data are provided with this paper.

References

1. Chambers, E. S. & Vukmanovic-Stejic, M. Skin barrier immunity and ageing. *Immunology* **160**, 116–125 (2020).
2. Vig, K. et al. Advances in skin regeneration using tissue engineering. *Int J. Mol. Sci.* **18**, 789 (2017).
3. Opneja, A., Kapoor, S. & Stavrou, E. X. Contribution of platelets, the coagulation and fibrinolytic systems to cutaneous. *Thromb. Res* **179**, 56–63 (2019).
4. Cañedo-Dorantes, L. & Cañedo-Ayala, M. Skin acute wound healing: a comprehensive review. *Int. J. Inflamm.* **2019**, 3706315 (2019).
5. Lei, H. & Fan, D. Conductive, adaptive, multifunctional hydrogel combined with electrical stimulation for deep wound repair. *Chem. Eng. J.* **421**, 129578 (2021).
6. Lv, Y. et al. Visible-light cross-linkable multifunctional hydrogels loaded with exosomes facilitate full-thickness skin defect wound healing through participating in the entire healing process. *ACS Appl. Mater. Interfaces* **16**, 25923–25937 (2024).
7. Singh, H. et al. Copper-MOF and tannic acid-empowered composite cryogel as a skin substitute for accelerated deep wound healing. *Biomater. Adv.* **164**, 213983 (2024).
8. Lou, P. et al. Extracellular vesicle-based therapeutics for the regeneration of chronic wounds: current knowledge and future perspectives. *Acta Biomater.* **119**, 42–56 (2021).
9. Castaño, O., Pérez-Amodio, S., Navarro-Requena, C., Mateos-Timoneda M & Engel, E. Instructive microenvironments in skin wound healing: biomaterials as signal releasing platforms. *Adv. Drug Deliv. Rev.* **129**, 95–117 (2018).
10. Oliva, N. & Almquist, B. D. Spatiotemporal delivery of bioactive molecules for wound healing using stimuli-responsive biomaterials. *Adv. Drug Deliv. Rev.* **161-162**, 22–41 (2020).
11. Yang, Y., Zhong, S., Meng, F. & Cui, X. Multi-functional hydrogels to promote diabetic wound healing: a review. *Chem. Eng. J.* **497**, 154855 (2024).
12. Fan, F., Saha, S. & Hanjaya-Putra, D. Biomimetic hydrogels to promote wound healing. *Front Bioeng. Biotechnol.* **9**, 718377 (2021).
13. Li, Y. et al. Multifunctional hydrogels prepared by dual ion cross-linking for chronic wound healing. *ACS Appl. Mater. Interfaces* **9**, 16054–16062 (2017).
14. Peña, O. A. & Martin, P. Cellular and molecular mechanisms of skin wound healing. *Nat. Rev. Mol. Cell Biol.* **25**, 599–616 (2024).
15. Lyu, S. et al. Going below and beyond the surface: microneedle structure, materials, drugs, fabrication, and applications for wound healing and tissue regeneration. *Bioact. Mater.* **27**, 303–326 (2023).
16. Duan, W. et al. Nanomaterials-incorporated polymeric microneedles for wound healing applications. *Int. J. Pharm.* **659**, 124247 (2024).
17. Legrand, J. M. D. & Martino, M. M. Growth factor and cytokine delivery systems for wound healing. *Cold Spring Harb. Perspect. Biol.* **14**, a041234 (2022).
18. Tang, L. et al. Platelet-derived growth factor nanocapsules with tunable controlled release for chronic wound healing. *Small* **20**, e2310743 (2024).
19. Long, L., Liu, W., Hu, C., Yang, L. & Wang, Y. Construction of multifunctional wound dressings with their application in chronic wound treatment. *Biomater. Sci.* **10**, 4058–4076 (2022).
20. Qiao, B. et al. ROS-responsive hydrogels with spatiotemporally sequential delivery of antibacterial and anti-inflammatory drugs for the repair of MRSA-infected wounds. *Regen. Biomater.* **11**, rbad110 (2024).
21. Nourian Dehkordi, A., Mirahmadi Babaheydari, F., Chehelgerdi, M. & Raeisi Dehkordi, S. Skin tissue engineering: wound healing based on stem-cell-based therapeutic strategies. *Stem Cell Res. Ther.* **10**, 111 (2019).
22. Savitri, C., Ha, S. S., Liao, E., Du, P. & Park, K. Extracellular matrices derived from different cell sources and their effect on macrophage behavior and wound healing. *J. Mater. Chem. B* **8**, 9744–9755 (2020).
23. Zeng, Q. K., Qi, X. L., Shi, G. Y., Zhang, M. & Haick, H. Wound dressing: from nanomaterials to diagnostic dressings and healing evaluations. *ACS Nano* **16**, 1708–1733 (2022).
24. Kucharzewski, M. et al. Novel trends in the application of stem cells in skin wound healing. *Eur. J. Pharmacol.* **843**, 307–315 (2019).
25. Guillamat-Prats, R. The role of MSC in wound healing, scarring and regeneration. *Cells* **10**, 1729 (2021).
26. Vizoso, F. J., Eiro, N., Cid, S., Schneider, J. & Perez-Fernandez, R. Mesenchymal stem cell secretome: toward cell-free therapeutic strategies in regenerative medicine. *Int. J. Mol. Sci.* **18**, 1852 (2017).
27. Di Santo, S. et al. Novel cell-free strategy for therapeutic angiogenesis: in vitro generated conditioned medium can replace progenitor cell transplantation. *PLoS One* **4**, e5643 (2009).
28. Murry, C. E. et al. Haematopoietic stem cells do not transdifferentiate into cardiac myocytes in myocardial infarcts. *Nature* **428**, 664–668 (2004).
29. Wang, C., Cheng, L., Xu, H. & Liu, Z. Towards whole-body imaging at the single cell level using ultra-sensitive stem cell labeling with oligo-arginine modified upconversion nanoparticles. *Biomaterials* **33**, 4872–4881 (2012).
30. Gnecchi, M. et al. Paracrine action accounts for marked protection of ischemic heart by Akt-modified mesenchymal stem cells. *Nat. Med.* **11**, 367–368 (2005).
31. Bian, D., Wu, Y., Song, G., Azizi, R. & Zamani, A. The application of mesenchymal stromal cells (MSCs) and their derivative exosome in skin wound healing: a comprehensive review. *Stem Cell Res. Ther.* **13**, 24 (2022).
32. Han, Y. et al. The secretion profile of mesenchymal stem cells and potential applications in treating human diseases. *Signal Transduct. Target Ther.* **7**, 92 (2022).
33. Pouya, S. et al. Study the effects of mesenchymal stem cell conditioned medium injection in mouse model of acute colitis. *Int. Immunopharmacol.* **54**, 86–94 (2018).
34. An, S. Y. et al. Milk fat globule-EGF factor 8, secreted by mesenchymal stem cells, protects against liver fibrosis in mice. *Gastroenterology* **152**, 1174–1186 (2017).
35. Takeuchi, R., Katagiri, W., Endo, S. & Kobayashi, T. Exosomes from conditioned media of bone marrow-derived mesenchymal stem cells promote bone regeneration by enhancing angiogenesis. *PLoS One* **14**, e0225472 (2019).
36. Chen, L. et al. Conditioned medium-electrospun fiber biomaterials for skin regeneration. *Bioact. Mater.* **6**, 361–374 (2021).

37. Liu, T. Y. et al. Controlled propulsion of micro/nanomotors: operational mechanisms, motion manipulation and potential biomedical applications. *Chem. Soc. Rev.* **51**, 10083–10119 (2022).
38. Ou, J. F. et al. Micro-/nanomotors toward biomedical applications: the recent progress in biocompatibility. *Small* **16**, e1906184 (2020).
39. Wang, S. N. et al. Biocompatibility of artificial micro/nanomotors for use in biomedicine. *Nanoscale* **11**, 14099–14112 (2019).
40. Zhang, D., Liu, S. Y., Guan, J. G. & Mou, F. Z. Motile-targeting" drug delivery platforms based on micro/nanorobots for tumor therapy. *Front. Bioeng. Biotechnol.* **10**, 1002171 (2022).
41. Mao, M., Wu, Y. J. & He, Q. Breaking through physiological barriers: nanorobotic strategies for active drug delivery. *Bioconjugate Chem.* **36**, 1–14 (2024).
42. Zheng, J. et al. Cascade-driven nanomotors promote diabetic wound healing by eradicating MRSA biofilm infection. *Chem. Eng. J.* **481**, 148790 (2024).
43. Wang, W. T. et al. Inflammatory microenvironment-responsive nanomotors with NIR photothermal effect for deep inflammation elimination and infection inhibition. *Adv. Funct. Mater.* **35**, 2416684 (2024).
44. Choi, H. et al. Microalgae-based biohybrid microrobot for accelerated diabetic wound healing. *Small* **19**, e2204617 (2023).
45. Lu, L. et al. Design and control of the magnetically actuated micro/nanorobot swarm toward biomedical applications. *Adv. Healthc. Mater.* **13**, e2400414 (2024).
46. Gwisai, T. et al. Magnetic torque-driven living microrobots for increased tumor infiltration. *Sci. Robot.* **7**, eabo0665 (2022).
47. Sun, M. et al. Magnetic microswarm and fluoroscopy-guided platform for biofilm eradication in biliary stents. *Adv. Mater.* **34**, e2201888 (2022).
48. Ye, Y. et al. Magnetically actuated biodegradable nanorobots for active immunotherapy. *Adv. Sci. (Weinh.)* **10**, e2300540 (2023).
49. Yan, C. et al. Biohybrid nanorobots carrying glycoengineered extracellular vesicles promote diabetic wound repair through dual-enhanced cell and tissue penetration. *Adv. Sci. (Weinh.)* **11**, e2404456 (2024).
50. Huang, S. et al. An improved protocol for isolation and culture of mesenchymal stem cells from mouse bone marrow. *J. Orthop. Transl.* **3**, 26–33 (2015).
51. Soleimani, M. & Nadri, S. A protocol for isolation and culture of mesenchymal stem cells from mouse bone marrow. *Nat. Protoc.* **4**, 102–106 (2009).
52. Nadri, S. et al. An efficient method for isolation of murine bone marrow mesenchymal stem cells. *Int. J. Dev. Biol.* **51**, 723–729 (2007).
53. Zhu, H. et al. A protocol for isolation and culture of mesenchymal stem cells from mouse compact bone. *Nat. Protoc.* **5**, 550–560 (2010).
54. Dong, Y. X., Wen, B., Chen, Y. J., Cao, P. Q. & Zhang, C. C. Autoclave-free facile approach to the synthesis of highly tunable nanocrystal clusters for magnetic responsive photonic crystals. *RSC Adv.* **6**, 64434–64440 (2016).
55. Wang, L. Y., Gu, Y. H., Su, Z. G. & Ma, G. H. Preparation and improvement of release behavior of chitosan microspheres containing insulin. *Int J. Pharm.* **311**, 187–195 (2006).
56. Luo, M. et al. Preparation and characterization of genipin-crosslinked chitosan microspheres for the sustained release of salidroside. *Int. J. Food Eng.* **11**, 323–333 (2015).
57. Yan, D. et al. Antimicrobial properties of chitosan and chitosan derivatives in the treatment of enteric infections. *Molecules* **26**, 7136 (2021).
58. Messina, J. M. et al. Unveiling cytokine charge disparity as a potential mechanism for immune regulation. *Cytokine Growth Factor Rev.* **77**, 1–14 (2024).
59. Dempsey, D. R., Jiang, H., Kalin, J. H., Chen, Z. & Cole, P. A. Site-specific protein labeling with n-hydroxysuccinimide-esters and the analysis of ubiquitin ligase mechanisms. *J. Am. Chem. Soc.* **140**, 9374–9378 (2018).
60. Li, X., Zeng, D. L., Ke, P., Wang, G. H. & Zhang, D. K. Synthesis and characterization of magnetic chitosan microspheres for drug delivery. *RSC Adv.* **10**, 7163–7169 (2020).
61. Ye, Z. & Sitti, M. Dynamic trapping and two-dimensional transport of swimming microorganisms using a rotating magnetic microrobot. *Lab Chip* **14**, 2177–2182 (2014).
62. Li, Z. W., Yang, F. & Yin, Y. D. Smart materials by nanoscale magnetic assembly. *Adv. Funct. Mater.* **30**, 1903467 (2020).
63. Yigit, B., Alapan, Y. & Sitti, M. Programmable collective behavior in dynamically self-assembled mobile microrobotic swarms. *Adv. Sci.* **6**, 1801837 (2019).
64. Liu, L. et al. Control the neural stem cell fate with biohybrid piezoelectrical magnetite micromotors. *Nano Lett.* **21**, 3518–3526 (2021).
65. Yang, M. Y. et al. Swarming magnetic nanorobots bio-interfaced by heparinoid-polymer brushes for in vivo safe synergistic thrombolysis. *Sci. Adv.* **9**, eadk7251 (2023).
66. Chen, L. et al. Correction: Conditioned medium from hypoxic bone marrow-derived mesenchymal stem cells enhances wound healing in mice. *PLoS One* **10**, e0145565 (2015).
67. Jiang, T., Wang, Z. & Sun, J. Human bone marrow mesenchymal stem cell-derived exosomes stimulate cutaneous wound healing mediates through TGF-β/Smad signaling pathway. *Stem Cell Res. Ther.* **11**, 198 (2020).
68. Wang, Z., Liu, W., Han, B., Yao, R. & Wei, C. Preparation of carboxymethyl-chitosan with different molecular weight and its effects on proliferation of skin fibroblasts and keratinocytes. *Sheng Wu Yi Xue Gong. Cheng Xue Za Zhi* **24**, 340–344 (2007).
69. Tchemtchoua, V. T. et al. Development of a chitosan nanofibrillar scaffold for skin repair and regeneration. *Biomacromolecules* **12**, 3194–3204 (2011).
70. Yang, C. K. et al. An injectable, self-healing, and antioxidant collagen- and hyaluronic acid-based hydrogel mediated with gallic acid and dopamine for wound repair. *Carbohydr. Polym.* **320**, 121231 (2023).
71. Pawitan, J. A. Prospect of stem cell conditioned medium in regenerative medicine. *Biomed. Res. Int.* **2014**, 965849 (2014).
72. Cosco, D. et al. Rutin-loaded chitosan microspheres: characterization and evaluation of the anti-inflammatory activity. *Carbohydr. Polym.* **152**, 583–591 (2016).
73. Du, M. Q. et al. Characterization and differentiation into adipocytes and myocytes of porcine bone marrow mesenchymal stem cells. *J. Integr. Agric.* **13**, 837–848 (2014).
74. Feyen, D. A. M. et al. Isolation of pig bone marrow-derived mesenchymal stem cells. *Methods Mol. Biol.* **1416**, 225–232 (2016).

Acknowledgements

This project was supported by the National Key Research and Development Program of China (2022YFA1206900, Y.T.), the National Natural Science Foundation of China (22175083, Y.T. and 22375224, F.P.), and the Public Welfare Technology Research Funding Project of Zhejiang (LTGY24H100002, S.W.).

Author contributions

Y.T. and J.J. proposed and designed the whole process of the study. J.J., H.L., Y.Y., W.H., J.M., H.X. Tan, Z.H., H. Tian, H.Q., X.Z., L.Z., and J.G. performed the experiments and analyzed the data. J.J. and Y.T. wrote the manuscript. Y.T., F.P., S.W. and X.S. supervised the project.

Competing interests

The authors declare no competing interests.

Additional information

Supplementary information The online version contains supplementary material available at https://doi.org/10.1038/s41467-025-61914-8.

Correspondence and requests for materials should be addressed to Xian Shen, Shuanghu Wang, Fei Peng or Yingfeng Tu.

Peer review information *Nature Communications* thanks the anonymous reviewers for their contribution to the peer review of this work. A peer review file is available.